An Operator Splitting Approach to the Solution of Fluid-Structure Interaction Problems in Hemodynamics

Martina Bukač, Sunčica Čanić, Boris Muha, and Roland Glowinski

Abstract We present a loosely coupled partitioned method for the numerical simulation of a class of fluid-structure interaction problems in hemodynamics. This method is based on a time discretization by an operator-splitting scheme of the Lie's type. The structure is assumed to be thin and modeled by the Koiter shell or membrane equations, while the fluid is modeled by the 3D Navier-Stokes equations for an incompressible viscous fluid. The fluid and structure are coupled via a full two-way coupling taking place at the moving fluid-structure interface, thus giving rise to a nonlinear moving-boundary problem. The Lie splitting decouples the fluid and structure sub-problems and is designed in such a way that the resulting partitioned scheme is unconditionally stable, without the need for any sub-iterations at every time step. Unconditional stability of the scheme is discussed using energy estimates, and several numerical examples are presented, showing that the scheme is first-order accurate in time. Implementation simplicity, computational efficiency, modularity, and unconditional stability make this scheme particularly appealing for solving FSI in hemodynamics.

Martina Bukač
Department of Applied and Computational Mathematics and Statistics, University of Notre Dame,153 Hurley Hall, Notre Dame, IN 46556, e-mail: mbukac@nd.edu

Sunčica Čanić
Department of Mathematics, University of Houston, 4800 Calhoun Rd., Houston TX 77025 e-mail: canic@math.uh.edu

Boris Muha
Department of Mathematics, Faculty of Science, University of Zagreb, Bijenicka 30, 10000 Zagreb, Croatia e-mail: borism@math.hr

Roland Glowinski
Department of Mathematics, University of Houston, 4800 Calhoun Rd. Houston TX 77025 e-mail: roland@math.uh.edu

1 Introduction

We consider the flow of an incompressible, viscous fluid in a 3D domain, see Figure 1, with compliant (elastic/viscoelastic) walls, which are assumed to be thin. The fluid flow is modeled by the 3D Navier-Stokes equations, while the elastodynamics of the structure, i.e., the elastic walls, is modeled by the Koiter shell, or membrane equations. The fluid and structure are coupled via a two-way coupling: the fluid in-

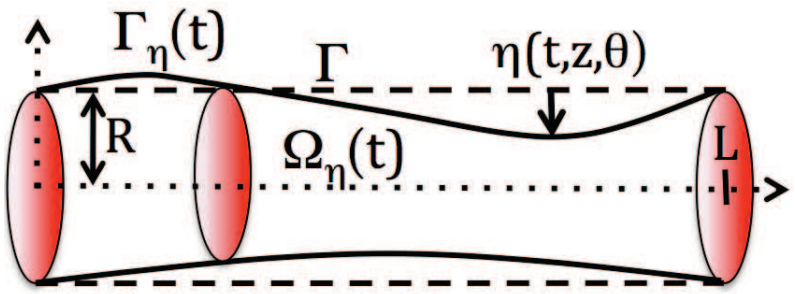

Fig. 1 Domain sketch and notation.

fluences the motion of the structure via the normal fluid stress, while the structure influences the motion of the fluid through the motion of the fluid domain boundary. This coupling is assumed through two coupling conditions: the kinematic coupling condition stating the continuity of velocity at the fluid-structure interface (the no-slip condition), and the dynamic coupling condition stating the second Newton's law of motion describing the elastodynamics of the thin structure loaded by the normal fluid stress. The resulting fluid-structure interaction (FSI) problem is a nonlinear moving-boundary problem.

This is a classical problem in hemodynamics describing the interaction between blood flow and elastic/viscoelastic arterial walls. The main difficulty in studying this problem stems from the fact that the fluid and structure have comparable densities, which is associated with the well-known added mass effect. The structure moves within the fluid as if an additional mass was added to it due to the presence of the surrounding fluid. Mathematically, this gives rise to a highly nonlinear moving-boundary problem, where the geometric nonlinearity due to the motion of the relatively light structure driven by the fluid of comparable density, needs to be resolved carefully. It is now well-known that this is the main reason for the instabilities in Dirichlet-Neumann loosely coupled schemes that are based on numerically solving this FSI problem by iterating once between the fluid and structure sub-problems [14], employing the Dirichlet boundary condition in the fluid sub-problem. The added mass effect, the associated geometric nonlinearities, and the multi-physics nature of the problem incorporating different physical effects (wave propagation v.s. diffusion) taking place at disparate time scales, are the main reasons why this

class of FSI problems remains to be challenging, both from the computational as well as theoretical points of view.

The development of numerical solvers for fluid-structure interaction problems has become particularly active since the 1980's [70, 71, 26, 34, 56, 62, 41, 40, 43, 42, 23, 48, 47, 54, 55, 74, 73, 3, 76, 25, 27, 52, 53, 20, 33].

Until recently, only monolithic algorithms seemed applicable to blood flow simulations [33, 36, 69, 79, 7, 8]. These algorithms are based on solving the entire nonlinear coupled problem as one monolithic system. They are, however, generally quite expensive in terms of computational time, programming time and memory requirements, since they require solving a sequence of strongly coupled problems using, e.g., fixed point and Newton's methods [58, 69, 22, 28, 47, 60].

The multi-physics nature of the blood flow problem strongly suggests to employ partitioned (or staggered) numerical algorithms, where the coupled fluid-structure interaction problem is separated into a fluid and a structure sub-problem. The fluid and structure sub-problems are integrated in time in an alternating way, and the coupling conditions are enforced asynchronously. When the density of the structure is much larger than the density of the fluid, as is the case in aeroelasticity, it is sufficient to solve, at every time step, just one fluid sub-problem and one structure sub-problem to obtain a solution. The classical loosely-coupled partitioned schemes of this kind typically use the structure velocity in the fluid sub-problem as Dirichlet data for the fluid velocity (enforcing the no-slip boundary condition at the fluid-structure interface), while in the structure sub-problem the structure is loaded by the fluid normal stress calculated in the fluid sub-problem. These Dirichlet-Neumann loosely-coupled partitioned schemes work well for problems in which the structure is much heavier than the fluid. Unfortunately, when fluid and structure have comparable densities, which is the case in blood flow applications, the simple strategy of separating the fluid from the structure suffers from severe stability issues [14, 61] associated with the added mass effect. The added mass effect reflects itself in Dirichlet-Neumann loosely coupled partitioned schemes by causing poor approximation of the total energy of the coupled problem at every time step of the scheme. A partial solution to this problem is to iterate several times between the fluid and structure sub-solvers at every time step until the energy of the continuous problem is well approximated. These strongly-coupled partitioned schemes, however, are computationally expensive and may suffer from convergence issues for certain parameter values [14].

To get around these difficulties, and to retain the main advantages of loosely-coupled partitioned schemes such as modularity, implementation simplicity, and low computational costs, several new loosely-coupled algorithms have been proposed recently. In general, they behave quite well for FSI problems containing a thin fluid-structure interface with mass [4, 9, 11, 44, 69, 29, 32, 30, 31, 1, 2, 5, 73, 67, 22, 21].

Recently, a novel loosely coupled partitioned scheme, called the Kinematically Coupled β-Scheme, was introduced by Bukač, Čanić et al. in [9, 11], and applied to 2D FSI problems with thin elastic and viscoelastic structures, modeled by the membrane or shell equations. This method was then extended to thick structure problems modeled by the equations of 2D elasticity [12], to 2D FSI problems with compos-

ite structures composed of multiple structural layers [65, 57], to 2D FSI problems with multiple poroelastic layers [10], FSI problems involving endovascular stents [63], and to an FSI problem with non-Newtonian fluids [59, 49]. This scheme deals successfully with the stability issues associated with the added mass effect in a way different from those reported above. Stability is achieved by combining the structure inertia with the fluid sub-problem to mimic the energy balance of the continuous, coupled problem. It was shown in [78] by considering a simplified problem, first used in [14] to study stability of loosely-coupled schemes, that our scheme is unconditionally stable for all $0 \leq \beta \leq 1$, even for the parameters associated with blood flow applications. Additionally, Muha and Čanić showed that a version of this scheme with $\beta = 0$ converges to a weak solution of the fully nonlinear FSI problem [64]. The case $\beta = 0$ considered in [64] corresponds to the classical kinematically-coupled scheme, first introduced in [44]. Parameter β was introduced in [9] to increase the accuracy of the scheme. A different approach to increasing the accuracy of the classical kinematically-coupled scheme was recently proposed by Fernández et al. [29, 32, 30]. Their modified kinematically-coupled scheme, called "the incremental displacement-correction scheme" treats the structure displacement explicitly in the fluid sub-step and then corrects it in the structure sub-step. Fernández et al. showed that the accuracy of the incremental displacement-correction scheme is first-order in time. The results were obtained for a FSI problem involving a thin elastic structure.

These recent results indicate that the kinematically-coupled scheme and its modifications provide an appealing way to study multi-physics problems involving FSI.

While all the results so far related to the kinematically-coupled β-scheme have been presented in 2D, here we show that this scheme, in combination with the Arbitrary Lagrangian-Eulerian approach, can successfully be extended to three space dimensions, and to problems without axial symmetry. We consider a FSI problem which consists of the 3D Navier-Stokes equations for an incompressible, viscous fluid, coupled with the linearly elastic Koiter membrane/shell equations. We show an energy estimate for the fully coupled nonlinear problem with $\beta = 0$, which, together with the convergence result of Muha and Čanić in [66], implies unconditional stability of the scheme. Using FreeFem++ [45, 46] we implemented the scheme for a few examples in 3D geometries: a 3D straight tube, a 3D curved tube, and a complex stenotic geometry which is not axially symmetric. We tested our solver against a monolithic solver on a 2D benchmark problem in blood flow [35], showing excellent agreement. Based on numerical results we show that the scheme has at least 1st-order accuracy in time both in 2D and 3D.

2 Model description

We consider the flow of an incompressible, viscous fluid in a three-dimensional cylindrical domain which is not necessarily axially symmetric. See Figure 1. We will be assuming that the lateral boundary of the cylinder is deformable and that

its location is not known *a priori*. The motion of the lateral boundary is fully coupled via a two-way coupling to the flow of the incompressible, viscous fluid occupying the fluid domain. Furthermore, it will be assumed that the lateral boundary is a thin, isotropic, homogeneous structure, whose displacement depends on both the axial variable z and on the azimuthal angle θ, thereby accounting for both axially-symmetric and non-axially symmetric displacements. Additionally, for simplicity, we will be assuming that only the radial component of displacement is non-negligible. The radial displacement from the reference configuration will be denoted by $\eta(t,z,\theta)$. See Figure 1. This is a common assumption in blood flow modeling [74]. *Neither the fluid flow, nor the displacement of the lateral boundary of the fluid domain will be required to satisfy the conditions of axial symmetry.*

Remark on notation: We will be using (z,x,y) to denote the Cartesian coordinates of points in $\mathbb{R}^3$, and (z,r,θ) to denote the corresponding cylindrical coordinates. We will be working with the fluid flow equations written in Cartesian coordinates, while the structure equations will be given in cylindrical coordinates. A function f given in Cartesian coordinates defines a function

$$\tilde{f}(z,r,\theta) = f(z,x,y)$$

defined in cylindrical coordinates. Since no confusion is possible, to simplify notation we will omit the superscript $\tilde{}$ and both functions, f and $\tilde{f}$, will be denoted by f.

The structural problem: Consider a clamped cylindrical shell of thickness h, length L, and reference radius of the middle surface equal to R. See Figure 1. This reference configuration, which we denote by Γ, can be defined via the parameterization

$$\varphi : \omega \to \mathbb{R}^3, \quad \varphi(z,\theta) = (R\cos\theta, R\sin\theta, z)^t,$$

where $\omega = (0,L)\times(0,2\pi)$ and $R > 0$. Therefore, the reference configuration is

$$\Gamma = \{\mathbf{x} = (R\cos\theta, R\sin\theta, z) \in \mathbb{R}^3 \ : \ \theta \in (0,2\pi), z \in (0,L)\}. \tag{1}$$

The associated covariant A_c and contravariant A^c metric tensors of this (undeformed) cylinder are give by:

$$\mathbf{A}_c = \begin{pmatrix} 1 & 0 \\ 0 & R^2 \end{pmatrix}, \ \mathbf{A}^c = \begin{pmatrix} 1 & 0 \\ 0 & \frac{1}{R^2} \end{pmatrix},$$

and the area element along cylinder Γ is $dS = \sqrt{a}dy := \sqrt{\det A_c}dy = Rdy$. The corresponding curvature tensor in covariant components is given by

$$\mathbf{B}_c = \begin{pmatrix} 0 & 0 \\ 0 & R \end{pmatrix}.$$

Under the action of force, the Koiter shell is deformed. The displacement from the reference configuration Γ of the deformed shell will be denoted by $\boldsymbol{\eta} = \boldsymbol{\eta}(t,z,\theta) = (\eta_z, \eta_\theta, \eta_r)$. We will be assuming that only the radial compo-

nent of the displacement is different from zero, and will be denoting that component of the displacement by $\eta(t,z,\theta) := \eta_r(t,z,\theta)$, so that $\boldsymbol{\eta} = \eta \mathbf{e}_r$, where $\mathbf{e}_r = \mathbf{e}_r(\theta) = (\cos\theta, \sin\theta, 0)^t$ is the unit vector in the radial direction.

The cylindrical Koiter shell is assumed to be clamped at the end points, giving rise to the following boundary conditions:

$$\eta = \frac{\partial \eta}{\partial \mathbf{n}} = 0 \text{ on } \partial\omega.$$

Deformation of a given Koiter shell depends on its elastic properties. The elastic properties of our cylindrical Koiter shell are defined by the following elasticity tensor $\mathscr{A}$:

$$\mathscr{A}\mathbf{E} = \frac{4\lambda\mu}{\lambda+2\mu}(\mathbf{A}^c \cdot \mathbf{E})\mathbf{A}^c + 4\mu \mathbf{A}^c \mathbf{E} \mathbf{A}^c, \quad \mathbf{E} \in \text{Sym}(\mathscr{M}_2), \tag{2}$$

where μ and λ are the Lamé coefficients. Using the following relationships between the Lamé constants and the Young's modulus of elasticity E and Poisson ratio σ:

$$\frac{2\mu\lambda}{\lambda+2\mu} + 2\mu = 4\mu\frac{\lambda+\mu}{\lambda+2\mu} = \frac{E}{1-\sigma^2}, \quad \frac{2\mu\lambda}{\lambda+2\mu} = 4\mu\frac{\lambda+\mu}{\lambda+2\mu}\frac{1}{2}\frac{\lambda}{\lambda+\mu} = \frac{E}{1-\sigma^2}\sigma, \tag{3}$$

the elasticity tensor $\mathscr{A}$ can also be written as:

$$\mathscr{A}\mathbf{E} = \frac{2E\sigma}{1-\sigma^2}(\mathbf{A}^c \cdot \mathbf{E})\mathbf{A}^c + \frac{2E}{1+\sigma}\mathbf{A}^c \mathbf{E} \mathbf{A}^c, \quad \mathbf{E} \in \text{Sym}\,(\mathscr{M}_2).$$

A Koiter shell can undergo stretching of the middle surface, and flexure (bending). Namely, the Koiter shell model accounts for both the membrane effects (stretching) and shell effects (flexure). Stretching of the middle surface is measured by the change of metric tensor, while flexure is measured by the change of curvature tensor. By assuming only the radial component of displacement $\eta = \eta(t,r,\theta)$ to be different from zero, the linearized change of metric tensor $\boldsymbol{\gamma}$, and the linearized change of curvature tensor $\boldsymbol{\rho}$, are given by the following:

$$\boldsymbol{\gamma}(\eta) = \begin{pmatrix} 0 & 0 \\ 0 & R\eta \end{pmatrix}, \quad \boldsymbol{\rho}(\eta) = \begin{pmatrix} -\partial_z^2\eta & -\partial_{z\theta}^2\eta \\ -\partial_{z\theta}^2\eta & -\partial_\theta^2\eta + \eta \end{pmatrix}. \tag{4}$$

With the corresponding change of metric and change of curvature tensors we can now formally write the corresponding elastic energy of the deformed shell [16, 17, 18, 51]:

$$E_{el}(\eta) = \frac{h}{4}\int_\omega \mathscr{A}\boldsymbol{\gamma}(\eta) : \boldsymbol{\gamma}(\eta) R dz d\theta + \frac{h^3}{48}\int_\omega \mathscr{A}\boldsymbol{\rho}(\eta) : \boldsymbol{\rho}(\eta) R dz d\theta, \tag{5}$$

where h is the thickness of the shell, and : denotes the inner product

$$\mathbf{A} : \mathbf{B} := \text{Tr}\left(\mathbf{A}\mathbf{B}^T\right) \ \mathbf{A}, \mathbf{B} \in \mathbf{M}_2(\mathbb{R}) \cong \mathbb{R}^4. \tag{6}$$

Given a force $\mathbf{f} = f\mathbf{e}_r$, with surface density f (the radial component), the loaded shell deforms under the applied force, and the corresponding displacement η is a solution to the following elastodyamics problem for the cylindrical linearly elastic Koiter shell, written in weak form: Find $\eta \in H_0^2(\omega)$ such that $\forall \psi \in H_0^2(\omega)$:

$$\begin{aligned}&\rho_K h \int_\omega \partial_t^2 \eta\, \psi R dz d\theta + \frac{h}{2}\int_\omega \mathscr{A}\boldsymbol{\gamma}(\eta) : \boldsymbol{\gamma}(\psi) R dz d\theta + \frac{h^3}{24}\int_\omega \mathscr{A}\boldsymbol{\rho}(\eta) : \boldsymbol{\rho}(\psi) R dz d\theta \\ &= \int_\omega f \psi R dz d\theta.\end{aligned} \tag{7}$$

The operator accounting for the elastic membrane and shell effects in the above equation will be denoted by $\mathscr{L}$:

$$\int_\omega \mathscr{L}\eta\, \psi R dz d\theta := \frac{h}{2}\int_\omega \mathscr{A}\boldsymbol{\gamma}(\eta) : \boldsymbol{\gamma}(\psi) R dz d\theta + \frac{h^3}{24}\int_\omega \mathscr{A}\boldsymbol{\rho}(\eta) : \boldsymbol{\rho}(\psi) R dz d\theta, \tag{8}$$

for all $\psi \in H_0^2(\omega)$, so that the above weak formulation can be written as

$$\rho_K h \int_\omega \partial_t^2 \eta\, \psi R dz d\theta + \int_\omega \mathscr{L}\eta\, \psi R dz d\theta = \int_\omega f \psi R dz d\theta,\ \forall \psi \in H_0^2(\omega). \tag{9}$$

A calculation shows that the operator $\mathscr{L}$, written in differential form, reads:

$$\begin{aligned}\mathscr{L}\eta = \frac{h^3\mu}{3R^3(\lambda+2\mu)}\Big((\lambda+\mu)\partial_\theta^4\eta + R^4(\lambda+\mu)\partial_z^4\eta + 2R^2(\lambda+\mu)\partial_z^2\partial_\theta^2\eta \\ - R^2\lambda\partial_z^2\eta - 2(\lambda+\mu)\partial_\theta^2\eta + (\lambda+\mu)\eta\Big) + \frac{4h}{R}\frac{(\lambda+\mu)\mu}{\lambda+2\mu}\eta.\end{aligned} \tag{10}$$

In terms of the Youngs modulus of elasticity, and the Poisson ratio, operator $\mathscr{L}$ can be written as:

$$\begin{aligned}\mathscr{L}\eta = \frac{h^3 E}{12R^4(1-\sigma^2)}\Big(\partial_\theta^4\eta + R^4\partial_z^4\eta + 2R^2\partial_z^2\partial_\theta^2\eta - 2\partial_\theta^2\eta + \eta\Big) \\ + \frac{h^3 E\sigma}{6R^2(1-\sigma^2)}\partial_z^2\eta + \frac{hE}{R^2(1-\sigma^2)}\eta.\end{aligned} \tag{11}$$

Thus, the elastodynamics of the cylindrical Koiter shell with only radial displacement different from zero, and without the assumption of axial symmetry, is modeled by

$$\rho_K h\frac{\partial^2\eta}{\partial t^2} + \mathscr{L}\eta = f, \tag{12}$$

where $\mathscr{L}$ is defined by (11), and η and f are functions of t, z, and θ, where η denotes the radial component of displacement.

If only the membrane effects are taken into account, the resulting cylindrical Koiter membrane model is given by:

$$\rho_K h\frac{\partial^2\eta}{\partial t^2}+\frac{hE}{R^2(1-\sigma^2)}\eta=f. \tag{13}$$

It was stated in [69, 19] that the general Koiter membrane model in *Cartesian coordinates*, with only normal displacement different from zero, takes the form:

$$\rho_K h\frac{\partial^2\eta}{\partial t^2}+C\eta=f, \tag{14}$$

where η here is the normal component of displacement in Cartesian coordinates, and the coefficient C is given by

$$C:=\frac{hE}{1-\sigma^2}(4\kappa_1^2-2(1-\sigma)\kappa_2), \tag{15}$$

where κ_1 and κ_2 are the mean and Gaussian curvature, respectively.

We mention one more reduced (thin-structure) model which has been used in modeling fluid-structure interaction in hemodynamics. The model was introduced in [33] by integrating the equations of linear elasticity defined on a cylindrical domain in 3D, with respect to the radial direction, after assuming that the material is homogeneous, isotropic, and that all the physical quantities, including the radial stress, are constant in the radial direction. In [33] this model was included in the fluid solver and solved using the so called *coupled momentum method*. The model was also studied in [13, 77]. It was shown in [77] that this model is well approximated by the following simplified membrane shell model:

$$\rho_K h\frac{\partial^2\eta}{\partial t^2}+C\eta-\frac{Eh}{2(1+\sigma)}\frac{\partial^2\eta}{\partial z^2}=f, \tag{16}$$

where C is given by (15), and η denoted the normal component of displacement in Cartesian coordinates. The model captures the membrane effects in Cartesian coordinates by the "spring term" $C\eta$, as well as wave propagation modeled by the second-order derivative term.

While the membrane models (13), (14) do not allow any boundary conditions to be imposed on the displacement at the "inlet" or "outlet" boundaries of the tube, model (16) requires two boundary conditions. This model will be considered in Section 5 where we impose zero displacement $\eta=0$, both at the inlet and outlet of the tube.

The fluid problem: The fluid domain, which depends on time and is not known *a priori*, will be denoted by

$$\Omega_\eta(t)=\{(z,x,y)\in\mathbb{R}^3:\sqrt{x^2+y^2}<R+\eta(t,z,\theta),\ z\in(0,L)\},$$

and the corresponding lateral boundary by

$$\Gamma_\eta(t)=\{(z,x,y)\in\mathbb{R}^3:\sqrt{x^2+y^2}=R+\eta(t,z,\theta),\ z\in(0,L)\}.$$

The corresponding reference cylinder is

$$\Omega = \{(z,x,y) \in \mathbb{R}^3 : \sqrt{x^2+y^2} < R,\ z \in (0,L)\}.$$

The lateral boundary of this cylinder, Γ, is defined in (1). The inlet and outlet sections of the fluid domain boundary will be denoted by $\Gamma_{in} = \{0\} \times (0,R)$, $\Gamma_{out} = \{L\} \times (0,R)$. See Figure 1.

The flow of an incompressible, viscous fluid in $\Omega_\eta(t)$ is modeled by the Navier-Stokes equations, which read, in Cartesian coordinates, as follows:

$$\left.\begin{aligned} \rho_f(\partial_t \mathbf{u} + \mathbf{u}\cdot\nabla\mathbf{u}) &= \nabla\cdot\sigma, \\ \nabla\cdot\mathbf{u} &= 0, \end{aligned}\right\} \text{ in } \Omega_\eta(t),\ t \in (0,T), \tag{17}$$

where ρ_f denotes the fluid density, $\mathbf{u}$ the fluid velocity, p the fluid pressure,

$$\sigma = -p\mathbf{I} + 2\mu_F \mathbf{D}(\mathbf{u})$$

is the fluid Cauchy stress tensor, μ_F is the kinematic viscosity coefficient, and $\mathbf{D}(\mathbf{u}) = \frac{1}{2}(\nabla\mathbf{u} + \nabla^t\mathbf{u})$ is the symmetrized gradient of $\mathbf{u}$.

At the inlet and outlet boundary we prescribe the normal stress via:

$$\boldsymbol{\sigma}\boldsymbol{n}_{in} = -p_{in}(t)\boldsymbol{n}_{in} \qquad \text{on } \Gamma_{in}\times(0,T), \tag{18}$$

$$\boldsymbol{\sigma}\boldsymbol{n}_{out} = -p_{out}(t)\boldsymbol{n}_{out} \qquad \text{on } \Gamma_{out}\times(0,T), \tag{19}$$

where $\boldsymbol{n}_{in}$ and $\boldsymbol{n}_{out}$ are the outward normals to the inlet and outlet fluid boundaries, respectively. Even though not physiologically optimal, these boundary conditions are common in blood flow modeling [4, 68].

Another set of boundary conditions, often helpful in the analysis of this FSI problem, is the dynamic pressure data with zero tangential velocity:

$$\left.\begin{aligned} p + \frac{\rho_f}{2}|u|^2 &= P_{in/out}(t), \\ \mathbf{u}\times\mathbf{e}_z &= 0, \end{aligned}\right\} \quad \text{on } \Gamma_{in/out}, \tag{20}$$

where $P_{in/out} \in L^2_{loc}(0,\infty)$ are given. It was shown in [66] that the FSI problem we study in this chapter, with the dynamics pressure data given by (20), has a weak solution.

Remark on the inlet and outlet data: In this chapter we will be using the normal stress inlet and outlet data in all the numerical examples, while the analysis of the stability of the scheme will be performed with the dynamic pressure inlet and outlet data.

The **coupling** between the fluid and structure is defined by two sets of boundary conditions satisfied at the lateral boundary $\Gamma_\eta(t)$. They are the kinematic and dynamic lateral boundary conditions describing continuity of velocity (the no-slip condition), and balance of contact forces (i.e., the Second Newton's Law of motion). Written in the Lagrangian framework, with $(z,\theta) \in \omega$, and $t \in (0,T)$, they read:

- **The kinematic condition:**

$$\partial_t \eta(t,z,\theta)\mathbf{e}_r(\theta) = \boldsymbol{u}(t,z,R+\eta(t,z,\theta),\theta), \tag{21}$$

where $\mathbf{e}_r(\theta) = (\cos\theta, \sin\theta, 0)^t$ is the unit vector in the radial direction.

- **The dynamic condition:**

$$\rho_K h\partial_t^2 \eta + \mathscr{L}\eta = -J(t,z,\theta)(\sigma\mathbf{n})|_{(t,z,R+\eta(t,z,\theta))} \cdot \mathbf{e}_r(\theta), \tag{22}$$

where $\mathscr{L}$ is defined by (10), or equivalently by (11), and

$$J(t,z,\theta) = \sqrt{(1+\partial_z\eta(t,z,\theta)^2)(R+\eta(t,z,\theta))^2 + \partial_\theta \eta(t,z,\theta)^2}$$

denotes the Jacobian of the composition of the transformation from Eulerian to Lagrangian coordinates and the transformation from cylindrical to Cartesian coordinates.

System (17)–(22) is supplemented with the following **initial conditions**:

$$\mathbf{u}(0,.) = \mathbf{u}_0,\ \eta(0,.) = \eta_0,\ \partial_t\eta(0,.) = v_0. \tag{23}$$

For regularity purposes, used in the existence proof presented in [66], we will be assuming that the initial data satisfies the following compatibility conditions:

$$\begin{gathered}\mathbf{u}_0(z,R+\eta_0(z),\theta)\cdot\mathbf{n}(z,\theta) = v_0(z,\theta)\mathbf{e}_r(\theta)\cdot\mathbf{n}(z,\theta), \quad z\in(0,L),\ \theta\in(0,2\pi),\\ \eta_0 = 0, \quad \text{on } \partial\omega,\\ R+\eta_0(z,\theta) > 0, \quad z\in[0,L],\ \theta\in(0,2\pi).\end{gathered} \tag{24}$$

Notice that the last condition requires that the initial displacement is such that the fluid domain has radius strictly greater than zero (i.e., the lateral boundary never collapses).

In summary, we study the following fluid-structure interaction problem:

Problem 1. Find $\mathbf{u} = (u_z(t,z,x,y), u_x(t,z,x,y), u_y(t,z,x,y))$, $p(t,z,x,y)$, and $\eta(t,z,\theta)$ such that

$$\left.\begin{aligned}\rho_f\left(\partial_t\mathbf{u} + (\mathbf{u}\cdot\nabla)\mathbf{u}\right) &= \nabla\cdot\sigma\\ \nabla\cdot\mathbf{u} &= 0\end{aligned}\right\} \text{ in } \Omega_\eta(t),\ t\in(0,T), \tag{25}$$

$$\left.\begin{aligned}\mathbf{u} &= \partial_t\eta\mathbf{e}_r,\\ \rho_K h\partial_t^2\eta + \mathscr{L}\eta &= -J\sigma\mathbf{n}\cdot\mathbf{e}_r,\end{aligned}\right\} \text{ on } \Gamma,\ t\in(0,T), \tag{26}$$

$$\left.\begin{aligned}\boldsymbol{\sigma}\boldsymbol{n}_{in} &= -p_{in}(t)\boldsymbol{n}_{in},\\ \boldsymbol{\sigma}\boldsymbol{n}_{out} &= -p_{out}(t)\boldsymbol{n}_{out},\end{aligned}\right\} \text{on } \Gamma_{in/out},\ t\in(0,T), \tag{27}$$

$$\left.\begin{aligned}\mathbf{u}(0,.) &= \mathbf{u}_0,\\ \eta(0,.) &= \eta_0,\\ \partial_t\eta(0,.) &= v_0.\end{aligned}\right\} \text{at } t=0. \tag{28}$$

This is a nonlinear, moving-boundary problem in 3D, which captures the full, two-way fluid-structure interaction coupling. The nonlinearity in the problem is represented by the quadratic term in the fluid equations, and by the nonlinear coupling between fluid and structure defined at the lateral boundary $\Gamma_\eta(t)$, which is one of the unknowns in the problem.

2.1 Energy inequality

To simplify notation, we introduce the following energy norms defined by the membrane and flexural effects of the linearly elastic Koiter shell:

$$\|f\|_\gamma := \int_\omega \mathscr{A}\boldsymbol{\gamma}(f) : \boldsymbol{\gamma}(f) R dz d\theta, \quad \|f\|_\sigma := \int_\omega \mathscr{A}\boldsymbol{\sigma}(f) : \boldsymbol{\sigma}(f) R dz d\theta. \tag{29}$$

Notice that norm $\|.\|_\gamma$ is equivalent to the standard $L^2(\omega)$ norm, and that norm $\|.\|_\sigma$ is equivalent to the standard $H_0^2(\omega)$ norm. Assuming sufficient regularity, and the inlet and outlet data given by a prescribed dynamic pressure, see (20), the following energy inequality holds:

Proposition 1. *Assuming sufficient regularity, and the inlet and outlet data given by a prescribed dynamic pressure, the solutions of* (25)*,* (26)*, and* (28) *satisfy the following energy estimate:*

$$\frac{d}{dt}\left(E_{kin}(t) + E_{el}(t)\right) + D(t) \leq C(P_{in}(t), P_{out}(t)), \tag{30}$$

where

$$\begin{aligned} E_{kin}(t) &:= \frac{1}{2}\left(\rho_f \|\mathbf{u}\|^2_{L^2(\Omega_\eta(t))} + \rho_K h \|\partial_t \eta\|^2_{L^2(\Gamma)}\right), \\ E_{el}(t) &:= \frac{h}{4}\|\eta\|_\gamma + \frac{h^3}{48}\|\eta\|_\sigma, \end{aligned} \tag{31}$$

denote the kinetic and elastic energy of the coupled problem, respectively, and the term $D(t)$ captures viscous dissipation in the fluid:

$$D(t) := \mu_F \|\mathbf{D}(\mathbf{u})\|^2_{L^2(\Omega_\eta(t))}. \tag{32}$$

The constant $C(P_{in}(t), P_{out}(t))$ depends only on the inlet and outlet pressure data, which are both functions of time.

The proof of inequality (30) is standard (see, e.g., [64]), so we omit it here. This says that if a smooth solution to the coupled fluid-structure interaction problem (25) - (28) exists, then it satisfies the energy inequality (30). This inequality states that the rate of change of the kinetic energy of the fluid, and the elastic energy of the structure, plus the viscous dissipation of the fluid, is balanced by the work done by the inlet and outlet data.

2.2 ALE Formulation

Since the fluid-structure coupling studied here is preformed along the moving fluid-structure interface, the fluid domain $\Omega(t)$ is not fixed. This is a problem from many points of view. In particular, defining the time discretization of the time derivative $\partial\mathbf{u}/\partial t$, for example $\partial\mathbf{u}/\partial t \approx (\mathbf{u}(t^{n+1},.)-\mathbf{u}(t^n,.))/(t^{n+1}-t^n)$, is not well-defined since $\mathbf{u}(t^{n+1},.)$ and $\mathbf{u}(t^n,.)$ are not defined on the same domain at two different time-steps. To resolve this difficulty, a classical approach is to map the fluid domain $\Omega_\eta(t)$ onto a fixed, reference domain Ω via a smooth, invertible ALE mapping [23]:

$$A_\eta : \Omega \to \Omega_\eta(t).$$

An example of such a mapping is the harmonic extension of the boundary $\partial\Omega_\eta(t)$ onto the fluid domain. This will be used in our numerical simulations. By using the chain rule, one can see that the the time derivative of the transformed fluid velocity will contain an additional advection term with its coefficient given by the domain velocity $\mathbf{w}^\eta := (A_\eta)_t \circ (A_\eta)^{-1}$, where $(A_\eta)_t$ denotes the time derivative of A_η.

Another example is an ALE mapping A_η defined by:

$$A_\eta(t) : \Omega \to \Omega_\eta(t), \quad A_\eta(t)(z,r,\theta) := \begin{pmatrix} z \\ (R+\eta(t,z,\theta))r \\ \theta \end{pmatrix}, \quad (z,r,\theta) \in \Omega, \tag{33}$$

where (z,r,θ) denote the cylindrical coordinates in the reference domain Ω. We will be using this explicit formula for ALE mapping in the energy estimate associated with the stability of our splitting scheme, proved in Section 3.2. Since we work with the Navier-Stokes equations written in Cartesian coordinates, it is useful to write an explicit form of the ALE mapping A_η in Cartesian coordinates as well:

$$A_\eta(t)(z,x,y) := \begin{pmatrix} z \\ (R+\eta(t,z,\theta))x \\ (R+\eta(t,z,\theta))y \end{pmatrix}, \quad (z,x,y) \in \Omega. \tag{34}$$

Mapping $A_\eta(t)$ is a bijection, and its Jacobian is given by

$$|\det \nabla A_\eta(t)| = (R+\eta(t,z,\theta))^2. \tag{35}$$

Composite functions with the ALE mapping will be denoted by

$$\mathbf{u}^\eta(t,.) = \mathbf{u}(t,.) \circ A_\eta(t) \quad \text{and} \quad p^\eta(t,.) = p(t,.) \circ A_\eta(t). \tag{36}$$

The derivatives of composite functions satisfy:

$$\nabla\mathbf{u} = \nabla\mathbf{u}^\eta (\nabla A_\eta)^{-1} =: \nabla^\eta \mathbf{u}^\eta, \quad \partial_t \mathbf{u} = \partial_t \mathbf{u}^\eta - (\mathbf{w}^\eta \cdot \nabla^\eta)\mathbf{u}^\eta,$$

where the ALE domain velocity, $\mathbf{w}^\eta$, is given by:

$$\mathbf{w}^\eta = \partial_t \eta \begin{pmatrix} 0 \\ x \\ y \end{pmatrix}. \tag{37}$$

The following notation will also be useful:

$$\sigma^\eta = -p^\eta \mathbf{I} + 2\mu \mathbf{D}^\eta(\mathbf{u}^\eta), \quad \mathbf{D}^\eta(\mathbf{u}^\eta) = \frac{1}{2}(\nabla^\eta \mathbf{u}^\eta + (\nabla^\eta)^\tau \mathbf{u}^\eta).$$

Finally, the mapped fluid equations in Ω_η read:

$$\left.\begin{aligned} \rho_F\left(\partial_t \mathbf{u} + ((\mathbf{u} - \mathbf{w}^\eta)\cdot\nabla^\eta)\mathbf{u}\right) &= \nabla^\eta \cdot \boldsymbol{\sigma}^\eta \\ \nabla^\eta \cdot \mathbf{u} &= 0 \end{aligned}\right\} \text{ in } \Omega_\eta(t)\times(0,T). \tag{38}$$

Here, the notation $\boldsymbol{\sigma}^\eta$ reflects the dependence of $\mathbf{D}^\eta(\mathbf{u}) = \frac{1}{2}(\nabla^\eta \mathbf{u} + \nabla^{\eta\,T}\mathbf{u})$ on η. Existence of a weak solution for problem (38), (26), (20), (28), was shown in [66]. In this chapter we focus on the design of a computational scheme for this problem. The computational scheme will follow the main steps in the proof, presented in [66], which is based on the Lie operator splitting approach.

The actual numerical simulations at each time step are typically performed on the current (fixed) domain $\Omega_\eta(t^n)$, at a given fixed time t^n, with only the time-derivative calculated on Ω, thereby avoiding the need to calculate the transformed gradients $\nabla^{\boldsymbol{\eta}}$. The corresponding continuous problem in ALE form can be written as follows:

Problem 2. Find $\mathbf{u}$, p, and η such that:

$$\left.\begin{aligned} \rho_F\left(\partial_t \mathbf{u}|_\Omega + ((\mathbf{u} - \mathbf{w}^\eta)\cdot\nabla)\mathbf{u}\right) &= \nabla\cdot\boldsymbol{\sigma} \\ \nabla\cdot\mathbf{u} &= 0 \end{aligned}\right\} \text{ in } \Omega_\eta(t)\times(0,T), \tag{39}$$

$$\left.\begin{aligned} \mathbf{u} &= \partial_t \eta \mathbf{e}_r, \\ \rho_K h \partial_t^2 \eta + \mathscr{L}\eta &= -J\sigma\mathbf{n}\cdot\mathbf{e}_r, \end{aligned}\right\} \text{ on } \Gamma,\ t\in(0,T), \tag{40}$$

$$\left.\begin{aligned} \boldsymbol{\sigma}\boldsymbol{n}_{in} &= -p_{in}(t)\boldsymbol{n}_{in}, \\ \boldsymbol{\sigma}\boldsymbol{n}_{out} &= -p_{out}(t)\boldsymbol{n}_{out}, \end{aligned}\right\} \text{on } \Gamma_{in/out},\ t\in(0,T), \tag{41}$$

$$\left.\begin{aligned} \mathbf{u}(0,.) &= \mathbf{u}_0, \\ \eta(0,.) &= \eta_0, \\ \partial_t\eta(0,.) &= v_0. \end{aligned}\right\} \text{at } t = 0. \tag{42}$$

Here, $\partial_t \mathbf{u}|_\Omega$ denotes the time derivative calculated on a reference domain Ω.

3 The Splitting Scheme

3.1 Description of the Splitting Scheme

To solve problem (39)-(42), we use the Lie or Marchuk-Yanenko splitting strategy. The Lie splitting is particularly useful for multi-physics problems like the one we are studying here. The coupled problem is split so that the different physics in the problem can be solved separately. The main difficulty is to design the Lie splitting strategy so that the resulting numerical scheme is stable and sufficiently accurate. We present here a splitting which leads to an unconditionally stable loosely coupled partitioned scheme. This splitting was first designed in [9] where a 2D benchmark problem was solved. In this chapter we extend this scheme to 3D problems, which, additionally, do not have to satisfy the property of axial symmetry.

It follows from [37] Chapter 6, that the Lie splitting scheme can be described as follows, the differential problem being written as a first-order system in time, namely:

$$\frac{\partial \phi}{\partial t} + F(\phi) = 0 \text{ in } (0,T), \tag{43}$$

$$\phi(0) = \phi_0, \tag{44}$$

where F is an operator from a Hilbert space into itself. Operator F is then split, in a non-trivial decomposition as

$$F = \sum_{i=1}^{I} F_i. \tag{45}$$

The problem is discretized in time by choosing the time step $\triangle t > 0$ and denoting $t^n = n\triangle t$, and $\phi^n = \phi(t^n)$. The initial approximation is given by the initial data $\phi^0 = \phi_0$. For $n \geq 0$, ϕ^{n+1} is computed by solving

$$\frac{\partial \phi_i}{\partial t} + F_i(\phi_i) = 0 \text{ in } (t^n, t^{n+1}), \tag{46}$$

$$\phi_i(t^n) = \phi^{n+(i-1)/I}, \tag{47}$$

then set $\phi^{n+i/I} = \phi_i(t^{n+1})$, for $i = 1, \ldots I$. Thus, the value at $t = t^{n+1}$ of the solution of the i-th problem is taken as the initial data for the $(i+1)$-st problem on (t^n, t^{n+1}).

This method is first-order accurate in time. More precisely, if (43) is defined on a finite-dimensional space, and if operators F_i are smooth enough, then $\|\phi(t^n) - \phi^n\| = O(\Delta t)$ [37].

To solve the FSI problem (39)-(42), we split the problem into two sub-problems as follows:

1. An elastodynamics problem for the structure, and
2. A fluid problem with suitable boundary conditions involving structure velocity and fluid stress at the boundary.

The structure and the fluid sub-problems are defined in such a way that the energy of the discretized problem approximates well the energy of the continuous problem. To achieve this goal, a key role is played by the kinematic coupling condition, which will be enforced implicitly in both steps of the splitting scheme, keeping the two sub-problems tightly coupled at all times. Indeed, we show below an energy estimate of the semi-discretized problem which is associated with unconditional stability of the scheme, and shows that the energy of the discretized problem mimics well the energy of the continuous problem.

More precisely, we begin by rewriting our coupled problem in first-order form with respect to time. For this purpose we introduce v to denote the trace of the fluid velocity at the moving interface $\Gamma(t)$:

$$v\mathbf{e_r} := \mathbf{u}|_{\Gamma(t)}.$$

The kinematic coupling condition (no-slip) then reads $\partial_t \eta = v$. The system in ALE form is now rewritten by using the above-mentioned notation, and by employing the *kinematic coupling condition* in the thin structure model. This way the kinematic coupling condition will be enforced implicitly everywhere, in all the steps of the splitting scheme. The resulting coupled problem in first-order ALE form is given by the following:

Problem 3. Find $\mathbf{u}$, p, η, and v such that:

$$\left.\begin{aligned} \rho_F\left(\partial_t \mathbf{u}|_\Omega + ((\mathbf{u}-\mathbf{w}^\eta)\cdot\nabla)\mathbf{u}\right) &= \nabla\cdot\boldsymbol{\sigma}, \\ \nabla\cdot\mathbf{u} &= 0, \end{aligned}\right\} \text{on } \Omega_\eta(t),\ t\in(0,T), \tag{48}$$

$$\left.\begin{aligned} \mathbf{u} &= v\mathbf{e}_r, \\ v &= \partial_t\eta, \\ \rho_K h\partial_t v + \mathscr{L}\eta &= -J\sigma\mathbf{n}\cdot\mathbf{e}_r, \end{aligned}\right\} \text{on } \Gamma,\ t\in(0,T), \tag{49}$$

$$\left.\begin{aligned} \boldsymbol{\sigma}\boldsymbol{n}_{in} &= -p_{in}(t)\boldsymbol{n}_{in}, \\ \boldsymbol{\sigma}\boldsymbol{n}_{out} &= -p_{out}(t)\boldsymbol{n}_{out}, \end{aligned}\right\} \text{on } \Gamma_{in/out},\ t\in(0,T), \tag{50}$$

$$\mathbf{u}^\eta(0,.) = \mathbf{u}_0, \eta(0,.) = \eta_0, v(0,.) = v_0, \quad \text{at} \quad t = 0. \tag{51}$$

We are now ready to split the problem. For this purpose, observe that the portion $\rho_K h\,\partial_t v = -J\boldsymbol{\sigma}\mathbf{n}\cdot\mathbf{e}_r$ of the dynamic coupling condition is formulated in terms of the trace v of the fluid velocity on Γ (recall that $\boldsymbol{\sigma}$ depends on v); we can, therefore, use this as the lateral boundary condition for the fluid sub-problem. This observation is crucial because keeping the structure inertia term $\rho_K h\partial_t v$ together with the inertia of the fluid in the fluid sub-problem is of paramount importance for designing a stable and convergent scheme. This mimics the added mass effect associated with the coupled physical problem, in which the coupled FSI solution dynamics corresponds to structure having combined fluid and structure inertia.

To achieve higher accuracy, we apply the following strategy: the normal fluid stress is split into two parts:

$$\boldsymbol{\sigma}\mathbf{n} = \underbrace{\boldsymbol{\sigma}\mathbf{n} + \beta p\mathbf{n}}_{(I)} \underbrace{- \beta p\mathbf{n}}_{(II)},$$

where $\beta \in [0,1]$, and part (I) is used in the fluid sub-problem, while part (II) in the structure sub-problem. The higher accuracy for $\beta > 0$ is achieved because the new splitting enhances the communication between the fluid and structure by loading the structure with a β portion of the normal fluid stress, which is not present for $\beta = 0$. For $\beta = 0$ we recover the classical kinematically-coupled scheme, first introduced in [44]. In this chapter, $\beta = 1$ is used for the numerical simulations since it provides the highest accuracy. The choice of β does not influence the stability of the scheme [9].

The operators F_1 and F_2 in the operator splitting scheme are defined by the following two differential sub-problems:

Problem F1 : **STRUCTURE**

$$\left.\begin{aligned} \partial_t \eta &= v, \\ \rho_K h \partial_t v + \mathscr{L}\eta &= \beta \hat{p}\mathbf{n}, \end{aligned}\right\} \text{ on } \Gamma,$$

Problem F2 : **FLUID**

$$\left.\begin{aligned} \partial_t \mathbf{u}|_\Omega + ((\hat{\mathbf{u}} - \mathbf{w}^\eta)\cdot\nabla)\mathbf{u} &= \nabla\cdot\boldsymbol{\sigma}, \\ \nabla\cdot\mathbf{u} &= 0, \end{aligned}\right\} \text{ in } \Omega_\eta(t),$$

$$\left.\begin{aligned} \mathbf{u}|_{R+\eta} &= v\mathbf{e}_r, \\ \rho_K h \partial_t v + J\boldsymbol{\sigma}\mathbf{n}|_{R+\eta} &= -\beta \hat{p}\mathbf{n}|_{R+\eta}. \end{aligned}\right\} \text{ on } \Gamma.$$

Here $\hat{\mathbf{u}}$ is the value of $\mathbf{u}$ from the previous time step, $\hat{p}$ is the value of p from the previous time step, and $\mathbf{w}^\eta$, which is the domain velocity (the time derivative of the ALE mapping), is obtained from the just calculated Problem F1. The initial data for $\mathbf{u}$ in the fluid domain is given by the solution from the previous time step, while the initial data for the trace v of the fluid velocity on Γ in Problem $F2$ is given by the just calculated velocity of the thin structure $\partial_t \eta$ in Problem $F1$. The corresponding operator splitting scheme is given by the block diagram shown in Figure 2.

This is different from the classical loosely coupled schemes. In classical Dirichlet-Neumann loosely coupled scheme, the boundary condition for the fluid subproblem is the Dirichlet condition for the fluid velocity v on Γ given in terms of the structure velocity $\partial\eta/\partial t$, namely $v = \partial\eta/\partial t$, where $\partial\eta/\partial t$ is *calculated at the previous time step*! This inclusion of the structure inertia from the previous time step (explicitly) makes the fluid subproblem unstable for certain parameters values [14]. The main reason for this is that the kinetic energy at this time step includes only the fluid kinetic energy from the current time step, and not the structure kinetic energy, since the thin structure velocity enters in an explicit way.

Therefore, our above-mentioned splitting strategy, that is to keep the thin structure inertia together with the fluid inertia in the fluid sub-step, respects the physical property of added mass effect in FSI problem where the fluid and structure have comparable densities, and will give rise to the kinetic energy of the discretized prob-

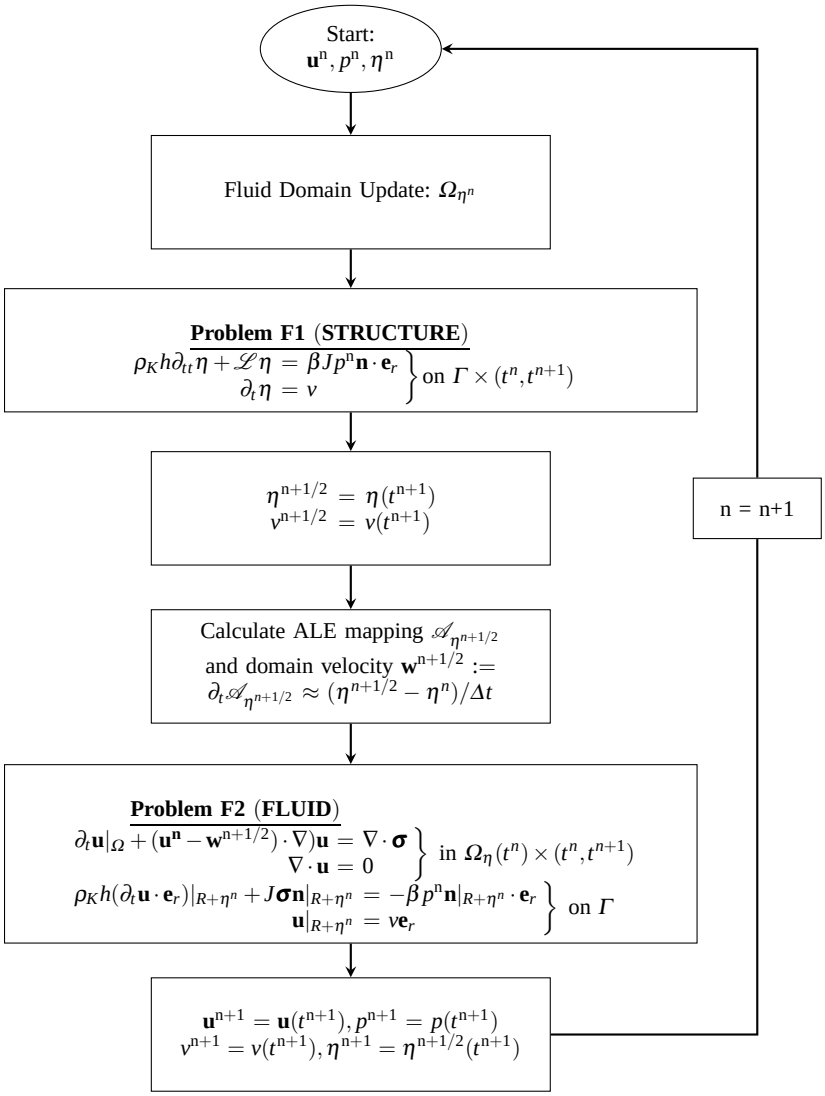

Fig. 2 A block diagram showing the main steps of the Kinematically Coupled β-Scheme.

lem which approximates well the kinetic energy of the continuous problem, as we will show next.

3.2 Unconditional Stability of the Splitting Scheme

We will show that the nonlinear FSI problem (39)-(42), semi-discretized via the Lie operator splitting described above, and summarized in the block diagram, shown in Figure 2, satisfies an energy estimate associated with unconditional stability of the operator splitting scheme. Combined with the compactness argument obtained in [66], which shows that the approximating (sub-)sequences of this splitting algorithm converge to a weak solution of problem (39)-(42), this estimate provides unconditional stability of the splitting scheme. This stability estimate is obtained for the problem containing the dynamic inlet and outlet pressure data (20).

To do this, we map the entire problem onto a fixed domain Ω via the ALE mapping (34), and perform the operator splitting, described above. The resulting structure elastodynamics problem and the fluid dynamics problem, written in weak form, are given by the following.

3.2.1 Problem F1: The structure elastodynamics problem

The weak form of a semi-discrete version of Problem F1 reads as follows:
• In this problem **u** does not change, and so

$$\mathbf{u}^{n+\frac{1}{2}} = \mathbf{u}^n;$$

• The functions $(v^{n+\frac{1}{2}}, \eta^{n+\frac{1}{2}}) \in H_0^2(\omega) \times H_0^2(\omega)$ are defined as solutions of the following problem, written in weak form, where we denote by $d\omega$ the measure $d\omega = Rdzd\theta$:

$$\begin{aligned} &\int_\omega \frac{\eta^{n+\frac{1}{2}} - \eta^n}{\Delta t}\phi\, d\omega = \int_\omega v^{n+\frac{1}{2}}\phi\, d\omega, \\ &\rho_K h \int_\omega \frac{v^{n+\frac{1}{2}} - v^n}{\Delta t}\psi d\omega + \frac{h}{2}\int_\omega \mathscr{A}\boldsymbol{\gamma}(\eta^{n+\frac{1}{2}}) : \boldsymbol{\gamma}(\psi) d\omega \\ &\qquad\qquad + \frac{h^3}{24}\int_\omega \mathscr{A}\boldsymbol{\rho}(\eta^{n+\frac{1}{2}}) : \boldsymbol{\rho}(\psi) d\omega = 0, \end{aligned} \tag{52}$$

for all $(\phi, \psi) \in L^2(\omega) \times H_0^2(\omega)$. The first equation is a weak form of the semi-discretized kinematic coupling condition, while the second equation corresponds to a weak form of the semi-discretized elastodynamics equation.

We will assume that the Lamé coefficients are such that operator $\mathscr{A}$ is coercive, e.g. $\lambda, \mu > 0$. It was shown in [66] that the following existence result and energy estimate hold for this problem.

Proposition 2. *For each fixed $\Delta t > 0$, problem* (52) *with $\lambda, \mu > 0$ has a unique solution $(v^{n+\frac{1}{2}}, \eta^{n+\frac{1}{2}}) \in H_0^2(\omega) \times H_0^2(\omega)$. Moreover, the solution of problem* (52) *satisfies the following discrete energy equality:*

$$E^{n+\frac{1}{2}}+\frac{1}{2}\Big(\rho_K h\|v^{n+\frac{1}{2}}-v^n\|^2+\frac{h}{2}\|\eta^{n+\frac{1}{2}}-\eta^n\|^2_\gamma+\frac{h^3}{24}\|\eta^{n+\frac{1}{2}}-\eta^n\|^2_\sigma\Big)=E^n, \tag{53}$$

where E^n denotes the kinetic energy of the fluid and structure, and the elastic energy of the Koiter shell of the n-th approximate solution:

$$E^n=\frac{1}{2}\Big(\rho_f\int_\Omega(R+\eta^n)^2|\mathbf{u}^n|^2d\boldsymbol{x}+\rho_K h\|v^n\|^2_{L^2(\omega)}+\frac{h}{2}\|\eta^n\|^2_\gamma+\frac{h^3}{24}\|\eta^n\|^2_\sigma\Big), \tag{54}$$

while $E^{n+1/2}$ is defined by:

$$E^{n+\frac{1}{2}}=\frac{1}{2}\Big(\rho_f\int_\Omega(R+\eta^n)^2|\mathbf{u}^{n+\frac{1}{2}}|^2d\boldsymbol{x}+\rho_K h\|v^{n+\frac{1}{2}}\|^2_{L^2(\omega)}+\frac{h}{2}\|\eta^{n+\frac{1}{2}}\|^2_\gamma+\frac{h^3}{24}\|\eta^{n+\frac{1}{2}}\|^2_\sigma\Big). \tag{55}$$

Notice how the three terms in (53) that are not included in the expressions E^n and $E^{n+1/2}$ account for the kinetic and elastic energy due to the motion of the fluid domain.

3.2.2 Problem F2: The fluid problem

We start by defining the solution space for the fluid velocity on the moving domain $\Omega_\eta(t)$ ([15, 39]):

$$\begin{aligned}\mathscr{V}_F(t)=\{\mathbf{u}=(u_z,u_x,u_y)\in H^1(\Omega_\eta(t))^3:\nabla\cdot\mathbf{u}=0,\\ \mathbf{u}\times\mathbf{e}_r=0 \text{ on } \Gamma(t),\ \mathbf{u}\times\mathbf{e}_z=0 \text{ on } \Gamma_{in/out}\},\end{aligned} \tag{56}$$

and then define the solution space for the fluid velocity defined on the mapped, fixed domain Ω by the following:

$$\mathscr{V}_F^\eta=\{\mathbf{u}^\eta(t,\cdot)=\mathbf{u}(t,\cdot)\circ\mathscr{A}_\eta(t):\mathbf{u}\in\mathscr{V}_F(t)\}.$$

It was shown in [66] that $\mathscr{V}_F^\eta$ is a Hilbert space with the scalar product:

$$\begin{aligned}(\mathbf{u}^\eta,\mathbf{v}^\eta)_{\mathscr{V}_F^\eta}&=\int_\Omega(R+\eta)^2\big(\mathbf{u}^\eta\cdot\mathbf{v}^\eta+\nabla^\eta\mathbf{u}^\eta:\nabla^\eta\mathbf{v}^\eta\big)d\boldsymbol{x}\\&=\int_{\Omega_\eta(t)}(\mathbf{u}\cdot\mathbf{v}+\nabla\mathbf{u}:\nabla\mathbf{v})d\boldsymbol{x}=(\mathbf{u},\mathbf{v})_{H^1(\Omega_\eta(t))}.\end{aligned}$$

The weak form of a semi-discrete version of Problem F2 reads as follows:
• In this problem η does not change, and so

$$\eta^{n+1}=\eta^{n+\frac{1}{2}};$$

• The function $(\mathbf{u}^{n+1},v^{n+1})\in\mathscr{V}_F^{\eta^n}\times L^2(\omega)$ is defined as a solution of the fluid sub-problem, written in weak form:

$$\rho_f \int_\Omega (R+\eta^n)^2 \left(\frac{\mathbf{u}^{n+1}-\mathbf{u}^{n+\frac{1}{2}}}{\Delta t} \cdot \mathbf{q} + \frac{1}{2}\left[(\mathbf{u}^n - \mathbf{w}^{n+\frac{1}{2}}) \cdot \nabla^{\eta^n} \right] \mathbf{u}^{n+1} \cdot \mathbf{q} \right.$$
$$\left. -\frac{1}{2}\left[(\mathbf{u}^n - \mathbf{w}^{n+\frac{1}{2}}) \cdot \nabla^{\eta^n} \right] \mathbf{q} \cdot \mathbf{u}^{n+1} \right) d\boldsymbol{x} + \rho_f \int_\Omega (R + \frac{\eta^n + \eta^{n+1}}{2}) v^{n+\frac{1}{2}} \mathbf{u}^{n+1} \cdot \mathbf{q}\, d\boldsymbol{x}$$
$$+2\mu \int_\Omega (R+\eta^n)^2 \mathbf{D}^{\eta^n}(\mathbf{u}^{n+1}) : \mathbf{D}^{\eta^n}(\mathbf{q})\, d\boldsymbol{x} + R\rho_K h \int_\omega \frac{v^{n+1}-v^{n+\frac{1}{2}}}{\Delta t} \psi dz d\theta$$
$$= P_{in}^n \int_{\Gamma_{in}} (q_z)_{|z=0} dx\, dy - P_{out}^n \int_{\Gamma_{out}} (q_z)_{|z=L} dx\, dy,$$
$$\text{with } \nabla^{\eta^n} \cdot \mathbf{u}^{n+1} = 0, \quad \mathbf{u}^{n+1}_{|\Gamma} = v^{n+1}\mathbf{e}_r, \tag{57}$$

for all $(\mathbf{q}, \psi) \in \mathscr{V}_F^{\eta^n} \times L^2(\omega)$ such that $\mathbf{q}_{|\Gamma} = \psi \mathbf{e}_r$.

Here $P_{in/out}^n = \frac{1}{\Delta t} \int_{n\Delta t}^{(n+1)\Delta t} P_{in/out}(t) dt$ and $\mathbf{w}^{n+\frac{1}{2}}$, which is the domain velocity defined via the ALE mapping (37), is given by

$$\mathbf{w}^{n+\frac{1}{2}} = v^{n+\frac{1}{2}} \begin{pmatrix} 0 \\ x \\ y \end{pmatrix}.$$

It was shown in [66] that the following existence result and energy estimate hold for this sub-problem:

Proposition 3. *Let $\Delta t > 0$, and assume that η^ns are such that $R + \eta^n \geq R_{\min} > 0, n = 0, ..., N$. Then, the fluid sub-problem defined by (57) has a unique weak solution $(\mathbf{u}^{n+1}, v^{n+1}) \in \mathscr{V}_F^{\eta^n} \times L^2(\omega)$. Moreover, the solution of (57) satisfies the following energy estimate:*

$$E^{n+1} + \frac{\rho_f}{2} \int_\Omega (R+\eta^n)^2 |\mathbf{u}^{n+1} - \mathbf{u}^n|^2 d\boldsymbol{x} + \frac{\rho_K h}{2} \|v^{n+1} - v^{n+\frac{1}{2}}\|^2_{L^2(\omega)}$$
$$+ D^{n+1} \leq E^{n+\frac{1}{2}} + C\Delta t ((P_{in}^n)^2 + (P_{out}^n)^2), \tag{58}$$

where P_{in}^n and P_{out}^n are the average inlet and outlet dynamic pressure data, given over the time interval (t^n, t^{n+1}): $P_{in/out} = \frac{1}{\Delta t} \int_{n\Delta t}^{(n+1)\Delta t} P_{in/out}(t) dt$, E^n is the kinetic and elastic energy defined in (54)*, and D^n, the contribution from fluid dissipation is defined by*

$$D^{n+1} = \Delta t \mu_F \int_\Omega (R+\eta^n)^2 |D^{\eta^n}(\mathbf{u}^{n+1})|^2 d\boldsymbol{x},\ n = 0, \ldots, N-1. \tag{59}$$

The constant C depends only on the parameters in the problem, and not on Δt.

By combining these two results we obtain an energy estimate for the semi-discretized problem in the following way. We begin by bounding the kinetic energy and the elastic energy at time step t^{n+1}:

$$
\begin{aligned}
&E^{n+1}+\frac{\rho_f}{2}\int_\Omega (R+\eta^n)^2|\mathbf{u}^{n+1}-\mathbf{u}^n|^2 d\boldsymbol{x}+\frac{\rho_K h}{2}\|v^{n+1}-v^n\|^2_{L^2(\omega)}\\
&\qquad +\frac{h}{4}\|\eta^{n+1}-\eta^n\|^2_\gamma+\frac{h^3}{48}\|\eta^{n+1}-\eta^n\|^2_\sigma+D^{n+1}\\
&\le E^{n+1}+\frac{\rho_f}{2}\int_\Omega (R+\eta^n)^2|\mathbf{u}^{n+1}-\mathbf{u}^n|^2 d\boldsymbol{x}+\frac{\rho_K h}{2}\|v^{n+1}-v^{n+\frac{1}{2}}\|^2_{L^2(\omega)}\\
&+\frac{\rho_K h}{2}\|v^{n+\frac{1}{2}}-v^n\|^2+\frac{h}{4}\|\eta^{n+1}-\eta^n\|^2_\gamma+\frac{h^3}{48}\|\eta^{n+1}-\eta^n\|^2_\sigma+D^{n+1}.
\end{aligned}
$$

We use the fact that $\eta^{n+1}=\eta^{n+\frac{1}{2}}$ in the last line to obtain that the above expression equals:

$$
\begin{aligned}
&=E^{n+1}+\frac{\rho_f}{2}\int_\Omega (R+\eta^n)^2|\mathbf{u}^{n+1}-\mathbf{u}^n|^2 d\boldsymbol{x}+\frac{\rho_K h}{2}\|v^{n+1}-v^{n+\frac{1}{2}}\|^2_{L^2(\omega)}\\
&+\frac{\rho_K h}{2}\|v^{n+\frac{1}{2}}-v^n\|^2+\frac{h}{4}\|\eta^{n+\frac{1}{2}}-\eta^n\|^2_\gamma+\frac{h^3}{48}\|\eta^{n+\frac{1}{2}}-\eta^n\|^2_\sigma+D^{n+1}.
\end{aligned}
$$

From the energy inequality (58) we can estimate the first line in the above expression by

$$
\begin{aligned}
&E^{n+\frac{1}{2}}+\frac{\rho_K h}{2}\|v^{n+\frac{1}{2}}-v^n\|^2+\frac{h}{4}\|\eta^{n+\frac{1}{2}}-\eta^n\|^2_\gamma+\frac{h^3}{48}\|\eta^{n+\frac{1}{2}}-\eta^n\|^2_\sigma\\
&\qquad +C\Delta t((P^n_{in})^2+(P^n_{out})^2),
\end{aligned}
$$

and by the energy equality (53), the above expression is equal to

$$
=E^n+C\Delta t((P^n_{in})^2+(P^n_{out})^2). \tag{60}
$$

Therefore, we have just shown that the split, semi-discretized problem satisfies the following energy estimate:

$$
\begin{aligned}
&E^{n+1}+\frac{\rho_f}{2}\int_\Omega (R+\eta^n)^2|\mathbf{u}^{n+1}-\mathbf{u}^n|^2 d\boldsymbol{x}+\frac{\rho_K h}{2}\|v^{n+1}-v^n\|^2_{L^2(\omega)}\\
&\qquad +\frac{h}{4}\|\eta^{n+1}-\eta^n\|^2_\gamma+\frac{h^3}{48}\|\eta^{n+1}-\eta^n\|^2_\sigma+D^{n+1}\\
&\qquad\qquad \le E^n+C\Delta t((P^n_{in})^2+(P^n_{out})^2).
\end{aligned} \tag{61}
$$

By using this estimate to further bound the right hand-side from the time level n all the way down to 0, and by recalling that P^n_{in} and P^n_{out} are the average inlet and outlet data over the time interval $(n\Delta t,(n+1)\Delta t)$, one obtains

$$
\begin{aligned}
&E^{n+1}+\frac{\rho_f}{2}\int_\Omega (R+\eta^n)^2|\mathbf{u}^{n+1}-\mathbf{u}^n|^2 d\boldsymbol{x}+\frac{\rho_K h}{2}\|v^{n+1}-v^n\|^2_{L^2(\omega)}\\
&\qquad +\frac{h}{4}\|\eta^{n+1}-\eta^n\|^2_\gamma+\frac{h^3}{48}\|\eta^{n+1}-\eta^n\|^2_\sigma+D^{n+1}\\
&\leq E_0+C\left\{\Delta t\sum_{n=0}^{N-1}\left(\frac{1}{\Delta t}\int_{n\Delta t}^{(n+1)\Delta t}P_{in}(t)dt\right)^2+\Delta t\sum_{n=0}^{N-1}\left(\frac{1}{\Delta t}\int_{n\Delta t}^{(n+1)\Delta t}P_{in}(t)dt\right)^2\right\}\\
&\qquad \leq E^0+C\|P_{in}\|^2_{L^2(0,T)}+\|P_{out}\|^2_{L^2(0,T)}.
\end{aligned}
\tag{62}
$$

We have just shown an energy estimate associated with the unconditional stability of the splitting scheme for the semi-discretized nonlinear FSI problem. Namely, the following theorem holds:

Theorem 1. *Under the assumption that the diameter of the fluid domain $\Omega_\eta(t)$ is greater than zero, the solutions of the semi-discrete splitting algorithm summarized in the block diagram of Figure 2 satisfy the following energy estimate:*

$$
\begin{aligned}
&E^{n+1}+\frac{\rho_f}{2}\int_\Omega (R+\eta^n)^2|\mathbf{u}^{n+1}-\mathbf{u}^n|^2 d\boldsymbol{x}+\frac{\rho_K h}{2}\|v^{n+1}-v^n\|^2_{L^2(\omega)}\\
&\qquad +\frac{h}{4}\|\eta^{n+1}-\eta^n\|^2_\gamma+\frac{h^3}{48}\|\eta^{n+1}-\eta^n\|^2_\sigma+D^{n+1}\\
&\qquad \leq E^0+C\|P_{in}\|^2_{L^2(0,T)}+\|P_{out}\|^2_{L^2(0,T)},
\end{aligned}
\tag{63}
$$

where the constant $C>0$ depends only on the parameters of the problem , E^0 is the kinetic and elastic energy of the initial data, and E^{n+1} denotes the kinetic and elastic energy of the semi-discretized solution at $t^{n+1}=(n+1)\Delta t$, defined by (54)*.*

Combined with the compactness arguments in [66], which show that the approximating sequence of the Lie splitting scheme converges strongly to a weak solution of the nonlinear FSI, the energy estimate (63) provides unconditional stability of the splitting scheme studied in this chapter.

4 The Numerical Implementation of the Scheme

In this section we present the details of the numerical scheme. As mentioned in Section 2 (**Remark on the inlet and outlet data**), in this section we use the normal stress inlet and outlet data (18), (19), to drive the problem.

4.1 The Structure Sub-Problem

The structure problem is discretized using the Backward Euler scheme, giving rise to the weak formulation of the structure sub-problem which is similar to the one presented in (52), except that (52) is presented for $\beta=0$ for which unconditional

stability is proved, and here we present this scheme for a general $\beta \in [0,1]$. More precisely, the structure sub-problem reads:
• In this sub-problem the fluid velocity in $\Omega(t^n)$ does not change, and so

$$\mathbf{u}^{n+\frac{1}{2}} = \mathbf{u}^n.$$

• Using the notation introduced in (8), the weak formulation for the cylindrical Koiter shell can be written as: Find $(v^{n+\frac{1}{2}}, \eta^{n+\frac{1}{2}}) \in L^2(\omega) \times H_0^2(\omega)$ such that $\forall (\phi, \psi) \in L^2(\omega) \times H_0^2(\omega)$:

$$\begin{aligned}
&\int_\omega \frac{\eta^{n+\frac{1}{2}} - \eta^n}{\Delta t} \phi R dz d\theta = \int_\omega v^{n+\frac{1}{2}} \phi R dz d\theta, \\
&\rho_K h \int_\omega \frac{v^{n+\frac{1}{2}} - v^n}{\Delta t} \psi R dz d\theta + \int_\omega \mathscr{L} \eta^{n+\frac{1}{2}} \psi R dr dz = \int_\omega \beta \tilde{p}^n J^n \psi R dz d\theta, \qquad (64) \\
&\text{with } v^n = \mathbf{u}^n|_{\Gamma^n},
\end{aligned}$$

where ω is the reference domain for the structure, $\mathscr{L}$ is defined in (8), and J^n is the Jacobian of the transformation from Eulerian to Lagrangian coordinates. Here, by $\tilde{p}^n$ we denoted the trace of the fluid pressure, calculated at time t^n, defined on the *reference configuration* ω via the ALE mapping $A^n : \Omega \to \Omega_{\eta^n}(t^n)$ as follows:

$$\tilde{p}^n = p^n \circ A^n. \qquad (65)$$

In the numerical implementation of the scheme, however, to avoid calculating the Jacobian J^n, the integral on the right hand-side can be calculated along the current configuration of the structure $\Gamma^n = \Gamma(t^n)$, so that

$$\int_\omega \beta \tilde{p}^n J^n \psi R dz d\theta = \int_{\Gamma^n} \beta p^n \psi dS^n, \qquad (66)$$

where dS^n is the surface element of Γ^n, and the functions p and $\tilde{p}$, are related through the ALE mapping A^n via (65). The same holds for the test functions: the ψ on the left hand side is defined on ω, while the test function ψ on the right hand-side is defined on Γ^n.

In the case when the Koiter shell equations are reduced to the membrane equation, all the terms multiplying $h^3/24$ are considered negligible, and the only term that survives is the non-differentiated term $C\eta$, so that the weak formulation reads: Find $(\eta^{n+\frac{1}{2}}, v^{n+\frac{1}{2}}) \in L^2(\omega) \times L^2(\omega)$ such that $\forall (\phi, \psi) \in L^2(\omega) \times L^2(\omega)$:

$$\begin{aligned}
&\int_\omega \frac{\eta^{n+\frac{1}{2}} - \eta^n}{\Delta t} \phi R dr dz = \int_\omega v^{n+\frac{1}{2}} \phi R dr dz, \\
&\rho_K h \int_\omega \frac{v^{n+\frac{1}{2}} - v^n}{\Delta t} \psi R dr dz + \int_\omega C \eta^{n+\frac{1}{2}} \psi R dr dz = \int_\omega \beta \tilde{p}^n J^n \psi R dr dz, \qquad (67) \\
&\text{with } v^n = \mathbf{u}^n|_{\Gamma^n}.
\end{aligned}$$

where ω is the reference domain for the structure, and $\mathbf{u}|_{\Gamma^n}$ is the trace of the fluid velocity on the fluid-structure interface calculated in the previous time-step. For the cylindrical Koiter membrane, the coefficient C is given by

$$C = \frac{hE}{R^2(1-\sigma^2)}.$$

For a smooth enough domain which is **not necessarily cylindrical**, the weak form in Cartesian coordinates reads: Find $(\eta^{n+\frac{1}{2}}, v^{n+\frac{1}{2}}) \in L^2(\Gamma) \times L^2(\Gamma)$

$$\begin{aligned}
&\int_\Gamma \frac{\eta^{n+\frac{1}{2}} - \eta^n}{\Delta t}\phi dS = \int_\Gamma v^{n+\frac{1}{2}}\phi dS,\ \forall \phi \in L^2_0(\Gamma),\\
&\rho_K h \int_\Gamma \frac{v^{n+\frac{1}{2}} - v^n}{\Delta t} dS + \int_\Gamma C\eta^{n+\frac{1}{2}}\psi dS = \int_\Gamma \beta \tilde{p}^n J^n \psi dS,\ \forall \psi \in L^2_0(\Gamma), \qquad (68)\\
&\text{with } v^n = \mathbf{u}^n|_{\Gamma^n},
\end{aligned}$$

where Γ is the reference configuration of the structure in Cartesian coordinates, and $\mathbf{u}|_{\Gamma^n}$ is the trace of the fluid velocity on the fluid-structure interface calculated in the previous time-step. The coefficient C is given by (see [69, 19]):

$$C := \frac{hE}{1-\sigma^2}(4\kappa_1^2 - 2(1-\sigma)\kappa_2), \qquad (69)$$

with κ_1 and κ_2 being the mean and Gaussian curvature, respectively. Function η here is the normal component of displacement written in Cartesian coordinates. As before, to avoid calculating the Jacobian J^n, the right hand-side of equation (68) can be calculated by converting everything to the current domain so that

$$\int_\Gamma \beta \tilde{p}^n J^n \psi dS = \int_{\Gamma^n} \beta p^n \psi dS^n. \qquad (70)$$

In the examples that follow, we will be using the membrane models, first in cylindrical coordinates, and then in Cartesian coordinates for a stenotic geometry which is not axially symmetric.

Since the structure displacement does not change in the fluid sub-problem, we define:

$$\eta^{n+1} = \eta^{n+\frac{1}{2}}.$$

4.2 Calculation of the ALE Mapping and ALE Velocity $\mathbf{w}^{n+1}$

Using the just-calculated new position of the thin structure we calculate the ALE mapping A^{n+1} associated with the new structure position as a harmonic extension of the boundary to the entire fluid domain:

$$\begin{aligned} \nabla^2 A^{n+1} &= 0 \quad \text{in } \Omega, \\ A^{n+1}|_{\Gamma} &= \eta^{n+1}, \\ A^{n+1}|_{\partial\Omega^f \setminus \Gamma} &= 0. \end{aligned}$$

Using this ALE mapping we calculate the new ALE velocity $\mathbf{w}$ via

$$\mathbf{w}^{n+1} = \frac{\partial A^{n+1}}{\partial t} = \frac{\partial \boldsymbol{x}}{\partial t} \approx \frac{\boldsymbol{x}^{n+1} - \boldsymbol{x}^n}{\Delta t},$$

which remains unchanged in the fluid sub-problem, below.

4.3 The Fluid Sub-Problem

We discretize the fluid problem using the Backward Euler scheme, giving rise to the following weak formulation: Find $(\mathbf{u}^{n+1}, p^{n+1}) \in V^f(t^n) \times Q(t^n)$ and $v^{n+1} \in L^2(\Gamma)$ such that for all $(\boldsymbol{\varphi}, q) \in V^f(t^n) \times Q(t^n)$ and $\psi \in L^2(\Gamma)$ satisfying $\boldsymbol{\varphi}|_{\Gamma^n} = [\boldsymbol{\varphi} \circ (A^n)^{-1}]|_{\Gamma} = \psi \boldsymbol{n}^f$, the following holds:

$$\begin{aligned} &\rho_f \int_{\Omega^f(t^n)} \frac{\mathbf{u}^{n+1} - \mathbf{u}^{n+\frac{1}{2}}}{\Delta t} \cdot \boldsymbol{\varphi} d\boldsymbol{x} + \rho_f \int_{\Omega^f(t^n)} ((\mathbf{u}^{n+\frac{1}{2}} - \mathbf{w}^{n+1}) \cdot \nabla) \mathbf{u}^{n+1} \cdot \boldsymbol{\varphi} d\boldsymbol{x} \\ &+ 2\mu_f \int_{\Omega^f(t^n)} \boldsymbol{D}(\mathbf{u}^{n+1}) : \boldsymbol{D}(\boldsymbol{\varphi}) d\boldsymbol{x} - \int_{\Omega^f(t^n)} p^{n+1} \nabla \cdot \boldsymbol{\varphi} d\boldsymbol{x} + \int_{\Omega^f(t^n)} q \nabla \cdot \mathbf{u}^{n+1} d\boldsymbol{x} \\ &+ \rho_s h_s \int_{\Gamma} \frac{v^{n+1} - v^{n+\frac{1}{2}}}{\Delta t} \cdot \psi dS = - \int_{\Gamma} J^n \beta \tilde{p}^n \psi dS \\ &+ \int_{\Gamma_{in}} p_{in}(t^{n+1}) \boldsymbol{\varphi}|_{z=0} \cdot \boldsymbol{n}^f \, dx \, dy - \int_{\Gamma_{out}} p_{out}(t^{n+1}) \boldsymbol{\varphi}|_{z=L} \cdot \boldsymbol{n}^f \, dx \, dy. \end{aligned} \tag{71}$$

Here, again, we can use (70) to simplify the calculation of the pressure integral over Γ in terms of the integral over Γ^n without the Jacobian J^n:

$$\int_{\Gamma} \beta \tilde{p}^n J^n \psi dS = \int_{\Gamma^n} \beta p^n \psi dS^n.$$

We employed FreeFem++ [45, 46] to solve this problem in 3D, using a finite element approach. Finite dimensional spaces of globally continuous piecewise affine functions (P_1) were used for the space approximation of the structure sub-problem (written in terms of velocity). Concerning the space approximation of the fluid sub-problems (the fluid advection and a quasi-Stokes problem), we proceeded as follows:

(i) Let us denote by $\mathscr{T}_h$ the finite element mesh used to approximate the fluid sub-problem (since we are in 3D, $\mathscr{T}_h$ consists of tetrahedra).
(ii) We divided each element of $\mathscr{T}_h$ into four tetrahedra by joining its center of mass to each of its four vertices, the resulting mesh being denoted by $\mathscr{T}_{h/4}$.

(iii) To approximate the pressure (resp. the velocity) we used globally continuous functions, piecewise affine over the elements of $\mathscr{T}_h$ (resp., $\mathscr{T}_{h/4}$).

The resulting approximation of the Stokes problem is known as the P_1 + bubble/P_1, and does not require stabilization (a detailed discussion of the P_1 + bubble/P_1 approximation, for 2D incompressible viscous flow, can be found in e.g., [37]; see also the references therein). For our simulations, the number of elements of $\mathscr{T}_h$ was of the order of $8,000$.

However, for the first example presented below, which is a 2D benchmark problem, we used our custom-made code. For this 2D problem, P_1 elements based approximations were used for the structure sub-problem, while the Bercovier-Pironneau method (also known, as mentioned before, as P_1-iso-P_2/P_1) was used to approximate the fluid sub-problem; again, no stabilization is needed with this approach where each triangle of the pressure mesh $\mathscr{T}_h$ is divided into four sub-triangles (by joining the edge mid-points) to define the twice finer mesh $\mathscr{T}_{h/2}$ used to approximate the velocity (see Chapter 5 of [37] for more details).

5 Numerical Examples

We begin by presenting a benchmark problem in hemodynamics. Our solver will be validated on this benchmark problem against a monolithic scheme, and the classical kinematically-coupled scheme ($\beta = 0$). We show that the accuracy of our operator splitting scheme with $\beta = 1$ is comparable to the accuracy of the monolithic scheme, and has higher accuracy than the classical kinematically-coupled scheme ($\beta = 0$). This benchmark problem is in 2D. The remaining examples presented here will be in 3D.

5.1 Example 1: A 2D benchmark problem.

We consider a classical test problem proposed by Formaggia et al. in [35]. This problem has been used in several works as a benchmark problem for testing the results of fluid-structure interaction algorithms in hemodynamics [6, 68, 5, 72, 44, 9]. The structure model for this benchmark problem is of the form

$$\rho_s h \frac{\partial^2 \eta_r}{\partial t^2} - kGh \frac{\partial^2 \eta_r}{\partial z^2} + \frac{Eh}{1-\sigma^2}\frac{\eta_r}{R^2} - \gamma \frac{\partial^3 \eta_r}{\partial z^2 \partial t} = f, \tag{72}$$

with absorbing boundary conditions at the inlet and outlet boundaries:

$$\frac{\partial \eta_r}{\partial t} - \sqrt{\frac{kG}{\rho_s}} \frac{\partial \eta_r}{\partial z} = 0 \quad \text{at } z = 0 \tag{73}$$

$$\frac{\partial \eta_r}{\partial t} + \sqrt{\frac{kG}{\rho_s}} \frac{\partial \eta_r}{\partial z} = 0 \quad \text{at } z = L. \tag{74}$$

Here $G = \frac{E}{2(1+\sigma)}$ is the *shear modulus* and k is the *Timoshenko shear correction factor*. The flow is driven by the time-dependent pressure data:

$$p_{in}(t) = \begin{cases} \frac{p_{max}}{2}\left[1 - \cos\left(\frac{2\pi t}{t_{max}}\right)\right] & \text{if } t \le t_{max} \\ 0 & \text{if } t > t_{max} \end{cases}, \quad p_{out}(t) = 0 \; \forall t \in (0, T), \tag{75}$$

where $p_{max} = 2 \times 10^4$ (dynes/cm^2) and $t_{max} = 0.005$ (s). The values of all the parameters in this model are given in Table 1. The problem was solved over the time interval $[0, 0.012]$ s, which is the time it takes the inlet pressure wave to reach the end of the tube.

Parameters	**Values**	**Parameters**	**Values**
Radius R (cm)	0.5	**Length** L (cm)	6
Fluid density ρ_f (g/cm^3)	1	**Dyn. viscosity** μ (poise)	0.035
Wall density ρ_s(g/cm^3)	1.1	**Wall thickness** h_s (cm)	0.1
Young's mod. E(dynes/cm^2)	0.75×10^6	**Poisson's ratio** σ	0.5
Shear mod. G(dynes/cm^2)	0.25×10^6	**Viscoelasticity** γ (poise cm)	0.01
Timoshenko factor k	1		

Table 1 Geometry, fluid and structure parameters for Example 5.1.

Propagation of the corresponding pressure pulse in 2D is shown in Figure 6.

The numerical results obtained using the kinematically-coupled β scheme with $\beta = 1$ were compared with the numerical results obtained using the classical kinematically coupled scheme (i.e., $\beta = 0$) proposed in [44], and the monolithic scheme proposed in [72]. Figures 3, 4 and 5 show the comparison between tube diameter, flow rate and mean pressure, respectively, at six different times.

These results were obtained with the same mesh as the one used for a monolithic scheme in [72], containing 31×11 $\mathbb{P}_1$ fluid velocity vertices. More preciesely, we used an iso-parametric version (thoroughly discussed in [37] Chapter 5; see also [38]) of the Bercovier-Pironneau element spaces, also known as $\mathbb{P}_1$-iso-$\mathbb{P}_2/\mathbb{P}_1$ approximation of the Stokes problem in which a coarse mesh (mesh size h_p) is used to approximate the pressure, and a twice finer mesh (mesh size $h_v = h_p/2$) is used for the velocity.

The time step used was $\triangle t = 10^{-4}$ which is the same as the time step used for the monolithic scheme, while the time step used for the kinematically coupled scheme in [44] was $\triangle t = 5 \times 10^{-5}$. It is well-known that splitting schemes require smaller time step due to the splitting error. However, the splitting studied in this

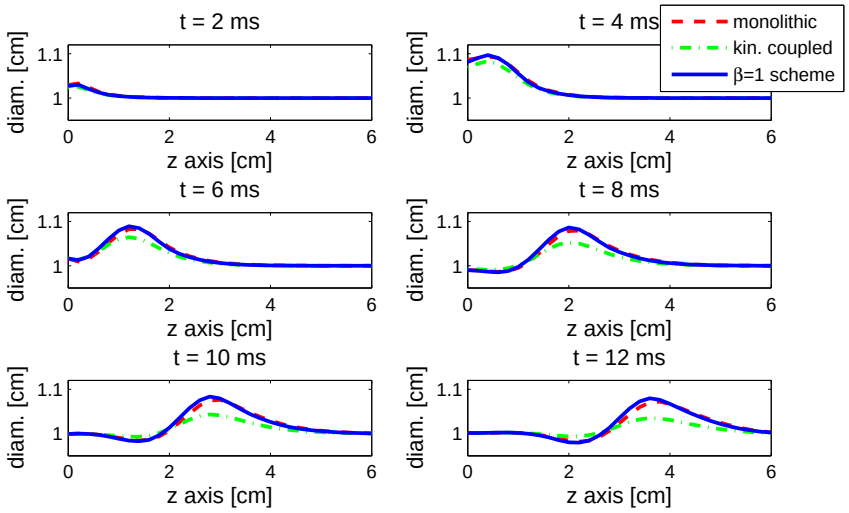

Fig. 3 Example 1: Diameter of the tube computed with the kinematically coupled scheme ($\beta = 0$) with time step $\triangle t = 5 \times 10^{-5}$ (dash-dot line), implicit scheme used by Quaini in [72] with the time step $\triangle t = 10^{-4}$ (dashed line), and the kinematically-coupled β-scheme ($\beta = 1$) with the time step $\triangle t = 10^{-4}$ (solid line).

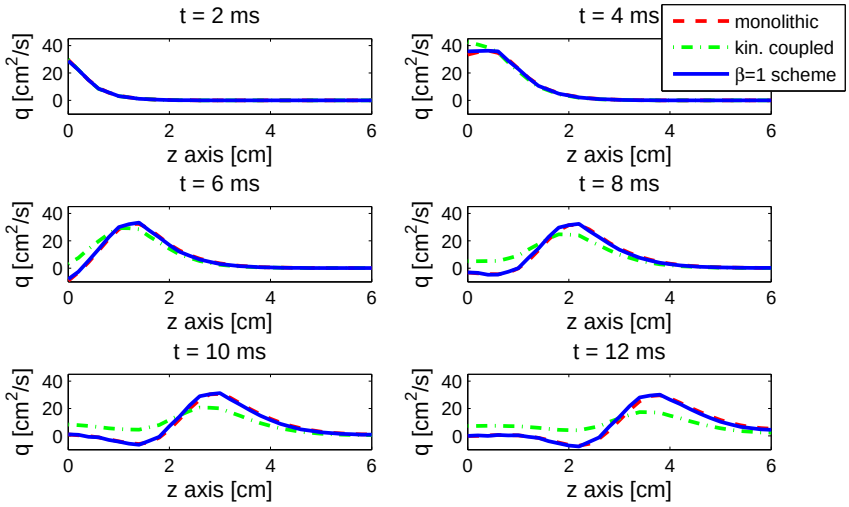

Fig. 4 Example 1: Flow rate computed with the kinematically coupled scheme ($\beta = 0$) with time step $\triangle t = 5 \times 10^{-5}$ (dash-dot line), the implicit scheme used by Quaini in [72] with the time step $\triangle t = 10^{-4}$ (dashed line), and our kinematically-coupled β-scheme ($\beta = 1$) with the time step $\triangle t = 10^{-4}$ (solid line).

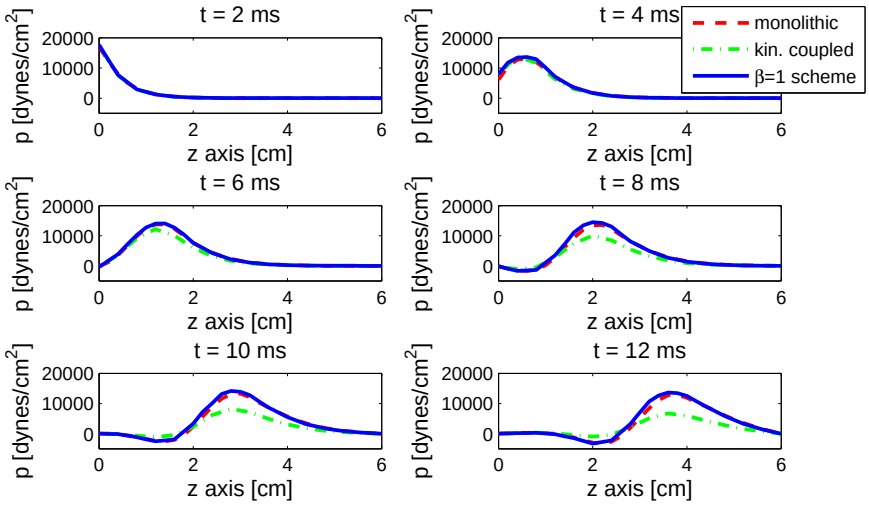

Fig. 5 Example 1: Mean pressure computed with the kinematically coupled scheme with time step $\triangle t = 5 \times 10^{-5}$ (dash-dot line), implicit scheme used by Quaini in [72] with the time step $\triangle t = 10^{-4}$ (dashed line) and our scheme with the time step $\triangle t = 10^{-4}$ (solid line).

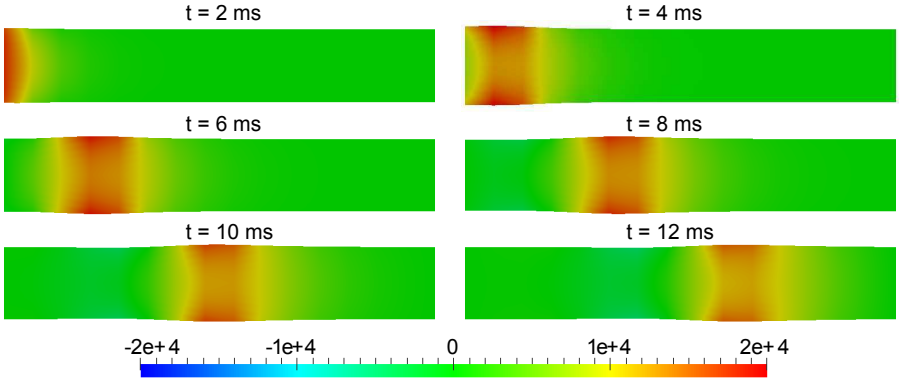

Fig. 6 Example 1: Propagation of the pressure wave.

chapter allows us to use the same time step as in the monolithic method, obtaining comparable accuracy, as it will be shown next. This is exciting since we obtain the same accuracy while retaining the main benefits of the partitioned schemes, such as modularity, implementation simplicity, and low computational cost.

Figure 7 shows a comparison between the time convergence of the kinematically-coupled β-scheme (with $\beta = 1$), the classical kinematically coupled scheme (i.e., $\beta = 0$), and the monolithic scheme used in [72]. The reference solution was defined to be the one obtained with $\triangle t = 10^{-6}$. We calculated the absolute L^2 error for the

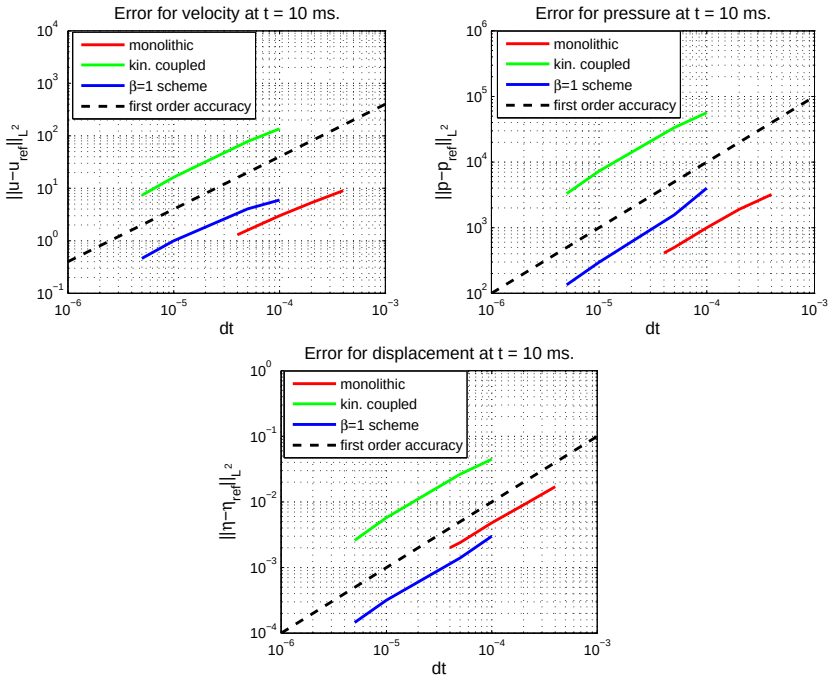

Fig. 7 Example 1: Log-log plot of errors for the three schemes. Left: Error for fluid velocity at t=10 ms. Middle: Error for fluid pressure at t=10 ms. Right: Error for displacement at t=10 ms.

$\triangle t$	$\|\|p-p_{ref}\|\|_{L^2}$	L^2 order	$\|\|\boldsymbol{u}-\boldsymbol{u}_{ref}\|\|_{L^2}$	L^2 order	$\|\|\boldsymbol{\eta}-\boldsymbol{\eta}_{ref}\|\|_{L^2}$	L^2 order
10^{-4}	4.01e+03	-	5.97	-	0.003	-
	(5.65e+04)	-	(136.32)	-	(0.0446)	-
5×10^{-5}	1.57e+03	1.35	4.05	0.56	0.0014	1.1
	(3.36e+04)	(0.75)	(77.91)	(0.80)	(0.0264)	(0.75)
10^{-5}	296.36	1.04	1.0	0.87	3.17e−04	0.92
	(7.27e+03)	(0.95)	(16.27)	(0.97)	(0.00576)	(0.95)
5×10^{-6}	134.33	1.14	0.46	1.12	1.45e−04	1.13
	(3.3e+03)	(1.14)	(7.36)	(1.14)	(0.0026)	(1.14)

Table 2 Example 1: Convergence in time calculated at $t = 10$ ms. The numbers in the parenthesis show the convergence rate for the kinematically coupled scheme ($\beta = 0$) presented in [44].

velocity, pressure and displacement between the reference solution and the solutions obtained using $\triangle t = 5\times10^{-6}, 10^{-5}, 5\times10^{-5}$ and 10^{-4}. Figure 7 shows first-order in time convergence for the velocity, pressure, and displacement obtained by the kinematically coupled scheme, monolithic scheme, and our scheme. Notice how the error of our method is comparable to the error obtained by the monolithic scheme on this 2D benchmark problem.

5.2 Example 2: A 3D Straight Tube Test Case

Here we study the flow in a straight, compliant 3D tube, whose elastodynamics is modeled by the cylindrical membrane shell equation (16). Notice that, in relation to the previous example, since the reference configuration is a straight cylinder, this model can be written as

$$\rho_s h \frac{\partial^2 \eta}{\partial t^2} - Gh \frac{\partial^2 \eta}{\partial z^2} + \frac{Eh}{1-\sigma^2} \frac{\eta}{R^2} = f, \tag{76}$$

where $G = \frac{E}{2(1+\sigma)}$ is the shear modulus, as in the previous example, and η denotes the radial component of displacement. We impose the zero-displacement boundary conditions $\eta = 0$ at the "inlet" and "outlet" boundary of the cylinder.

The flow is driven by the time-dependent pressure (normal stress) data:

$$p_{in}(t) = \begin{cases} \frac{p_{max}}{2}\left[1 - \cos\left(\frac{2\pi t}{t_{max}}\right)\right] & \text{if } t \le t_{max} \\ 0 & \text{if } t > t_{max} \end{cases}, \quad p_{out}(t) = 0 \; \forall t \in (0,T), \tag{77}$$

where $p_{max} = 1.3333 \times 10^4$ (dyne/cm^2) and $t_{max} = 0.003$ (s). The values of all the parameters in this model are given in Table 3.

Fluid Parameters	**Values**
Tube length L(cm)	5
Tube radius R(cm)	0.5
Fluid density ρ(g/cm^3)	1
Fluid viscosity μ(poise)	0.035

Structure Parameters	**Values**
Thickness h(cm)	0.1
Density ρ(g/cm^3)	1.1
Youngs modulus E(dyns/cm^2)	10^6
Poisson ratio σ	0.5

Table 3 Example 1: The structure parameters for Example 1.

The value of the time step is $\Delta t = 10^{-4}$, and the finite element approximation contains 8571 degrees of freedom.

In contrast with the previous example, the cylindrical membrane model does not contain the bending rigidity term(s), described by the second-order spatial derivative term in (72), which is associated with wave propagation phenomena, making equation (72) of hyperbolic type (assuming $\gamma = 0$). As a result, the pressure wave and displacement look slightly different in this example when compared with the previous example, as shown in Figures 8 – 11.

In particular, Fig. 8 shows the 3D tube with the corresponding pressure wave propagation at four different times within the time interval from $t = 0$ until $t =$ 14 milliseconds, which is the time it takes the pressure wave to reach the outlet boundary. The corresponding values of the pressure along the symmetry axis of the tube are shown in Fig. 9.

Similarly, Fig. 10 shows the magnitude of displacement along the 3D tube, at the same four time snap-shots as used in Figs. 8 and 9. The corresponding values

of the displacement along the symmetry axis of the tube are shown in Fig. 11. One can see how the energy dissipates very quickly in this case, and the amplitude of displacement decreases along the tube. The results in Figures 8 – 11 are very similar to the results reported in [69], where a pressure wave propagation was shown in a semicircular tube, modeled by the membrane model (14), (15).

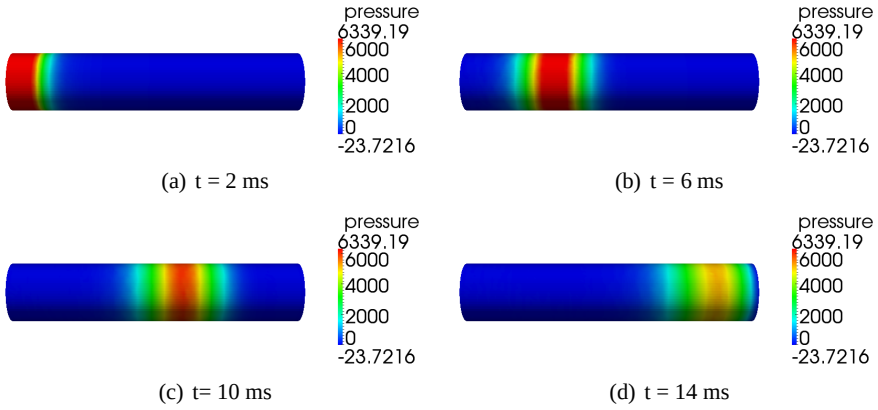

(a) t = 2 ms (b) t = 6 ms

(c) t= 10 ms (d) t = 14 ms

Fig. 8 Example 2: Pressure wave propagation in a 3D cylindrical tube, modeled by the cylindrical membrane equation (72).

We studied the time-convergence of the scheme solving this 3D problem by refining the time step from $\Delta t = 10^{-4}, 5\times 10^{-5}, 10^{-5}$, with the reference solution corresponding to the one obtained with $\Delta t = 5\times 10^{-6}$. Figure 12 shows the log-log plot of the error for the fluid velocity versus the time step. A table with the corresponding numbers, showing an "almost" second order convergence, is given in Table 5.2.

$\triangle t$	$\|\|\boldsymbol{u}-\boldsymbol{u}_{ref}\|\|_{L^2}$	Conv. Order
10^{-4}	0.71614	–
5×10^{-5}	0.201347	1.83
10^{-5}	0.0122303	1.74

Table 4 Example 2: A table showing an "almost" second order convergence.

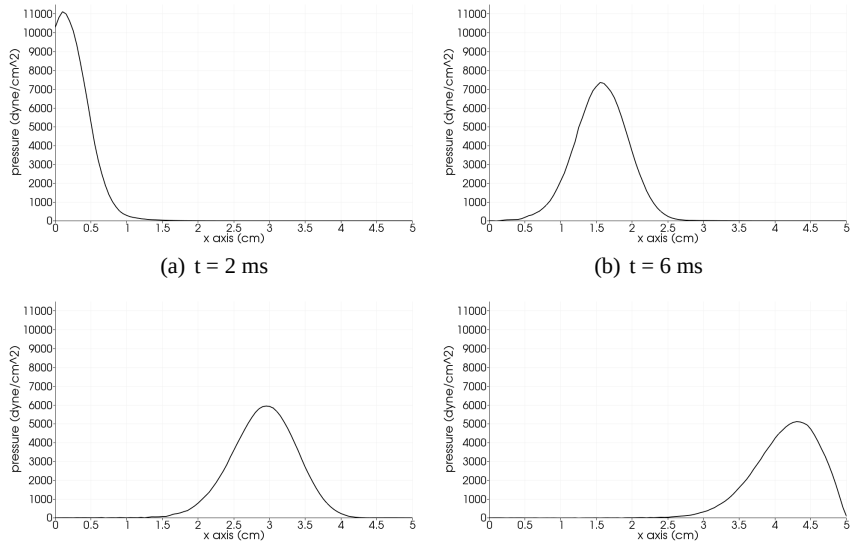

(a) t = 2 ms (b) t = 6 ms

(c) t= 10 ms (d) t = 14 ms

Fig. 9 Example 2: Pressure along the axis of symmetry of the tube corresponding to Fig. 8.

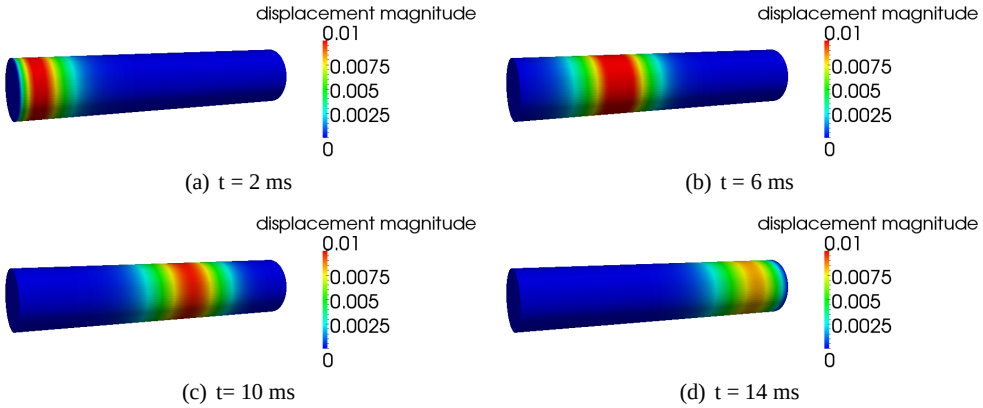

(a) t = 2 ms (b) t = 6 ms

(c) t= 10 ms (d) t = 14 ms

Fig. 10 Example 2: Displacement of the 3D cylindrical elastic tube from Figure 8.

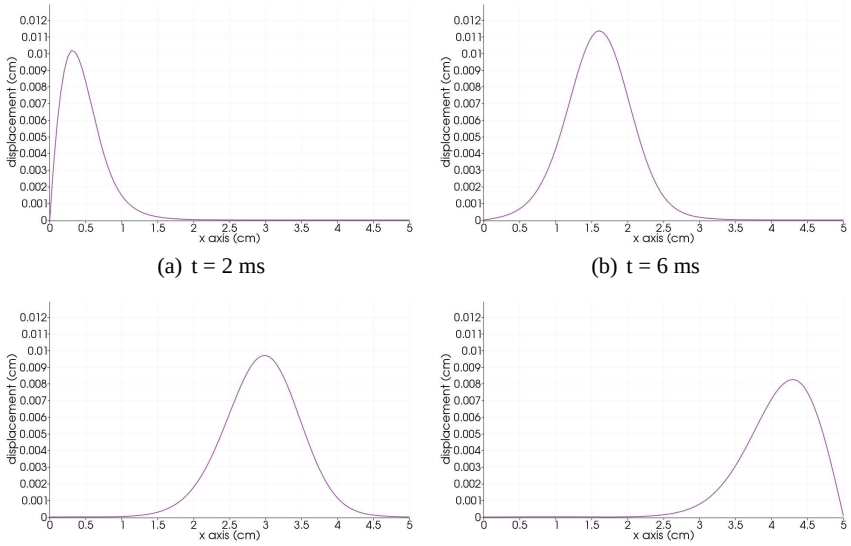

(a) t = 2 ms (b) t = 6 ms

(c) t=10 ms (d) t = 14 ms

Fig. 11 Example 2: Displacement along the tube axis corresponding to Fig. 10.

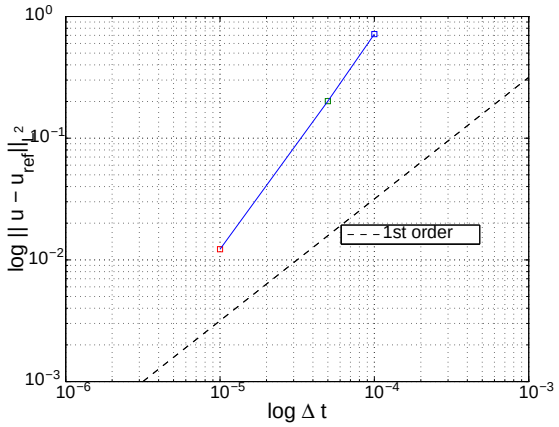

Fig. 12 Example 2: The time-convergence test showing the accuracy of order larger than 1. The dashed line in the figure shows the slope corresponding to 1st-order accuracy.

5.3 Example 3: A 3D Curved Cylinder

Here we consider the structure model (16) with C given by (15), where η denotes the normal component of displacement. For completeness, we state the model here:

$$\rho_K h \frac{\partial^2 \eta}{\partial t^2} - \frac{Eh}{2(1+\sigma)} \frac{\partial^2 \eta}{\partial z^2} + \frac{hE}{1-\sigma^2}(4\kappa_1^2 - 2(1-\sigma)\kappa_2)\eta = f, \qquad (78)$$

where κ_1 and κ_2 are the mean and Gaussian curvature, respectively. The reference domain is now a semicircular tube, approximating an idealized geometry of the ascending/descending aorta.

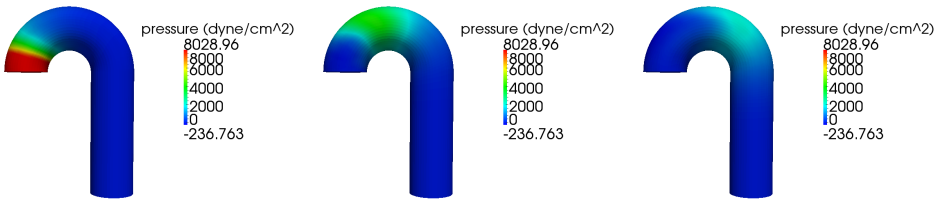

(a) t = 2 ms (b) t = 4 ms (c) t = 7 ms

Fig. 13 Example 3: Pressure wave propagation along the axis of symmetry of the curved tube.

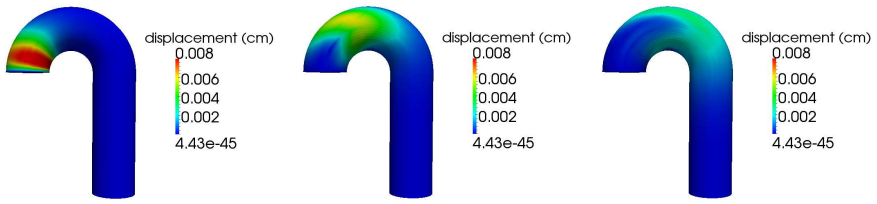

(a) t = 2 ms (b) t = 4 ms (c) t = 7 ms

Fig. 14 Example 3: Displacement of the curved tube.

The diameter of the cylinder is constant and equal to $R = 0.5$cm, while the two principal curvatures are given by $4\cos(\theta)/(2+\cos(\theta))$ for $\theta \in [0, 2\pi)$ (Gaussian curvature), and $2(1+\cos(\theta))/(2+\cos(\theta)), \theta \in [0, 2\pi)$ (mean curvature) for the portion of the domain that corresponds to a torus [50]. The other parameters are the same as in the above example, and are given in Table 3. Figures 13 and 14 show the pressure and displacement in the curved cylinder. They are very similar to the results obtained by Nobile and Vergara in [69] using the membrane model as a Robin boundary condition in the fluid problem.

5.4 Example 4: Stenosis

In this example we consider a stenotic geometry which is not axially symmetric. Fig. 15 shows two views of the geometry: the axial view and the cross-sectional

view, cut by plane A, shown inFig. 15. The corresponding computational mesh is also shown in this figure. The cross-section in Figure 15 (b) shows around 50% stenosis of the vessel lumen.

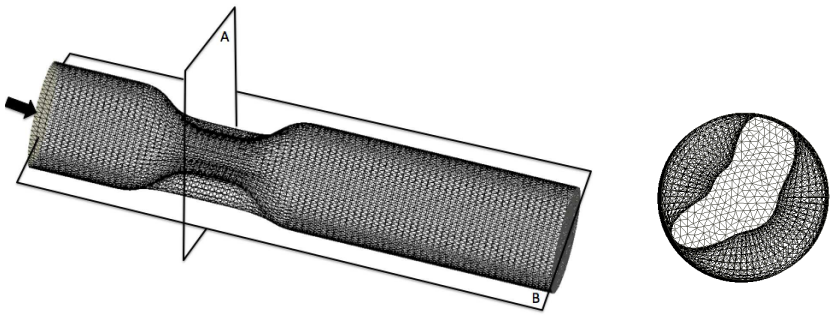

(a) Axial view of stenotic domain. (b) Cross-section A.

Fig. 15 Example 4: Stenotic geometry and computational mesh: longitudinal view (left) and cross-sectional view (right) obtained from the figure on the left by cutting the mesh geometry by the plane denoted in the figure on the left by A, and looking at the mesh from the center of the longitudinal axis, shown by the arrow in the figure on the left.

The structure elastodynamics is modeled by equation (79), where the coefficients now depend on the spatial variable **x**, since the radius and curvature of the reference configuration are not constant:

$$\rho_K h\frac{\partial^2\eta}{\partial t^2} - \frac{Eh}{2(1+\sigma)}\frac{\partial^2\eta}{\partial z^2} + \frac{hE}{1-\sigma^2}(4\kappa_1(\boldsymbol{x})^2 - 2(1-\sigma)\kappa_2(\boldsymbol{x}))\eta = f, \qquad (79)$$

Thus, the structure model and the coupling conditions have to be modified accordingly, as studied in [75]. The remaining values of the fluid and structure parameters are the same as in the previous example, and are shown in Table 3. The time step for the simulation is $\Delta t = 10^{-4}$.

Figs. 16, 17, 18, and 19 show the numerical solution for the velocity, pressure, and displacement, at different times. In particular, Fig. 16 shows 2D velocity snap shots taken at 4 different times. The 2D velocity snap shots are taken at the cross-section of the 3D domain by the plane denoted by B in Fig. 15. Fig. 17 shows the velocity at the throat, taken at $t = 7$ ms when the velocity reaches its maximum at the throat. The 2D velocity cross-section is taken in the plane denoted by A in Fig. 15. Fig. 16 shows the beginning rush of fluid into the tube ($t = 4$ ms), the acceleration of the fluid at the proximal throat location ($t = 7$ ms), the high velocity region at the distal location of the stenotic throat ($t = 10$ ms), and the velocity ahead of the pressure wave exiting the tube ($t = 13$ ms). The corresponding pressure wave propagation is shown in Fig. 18.

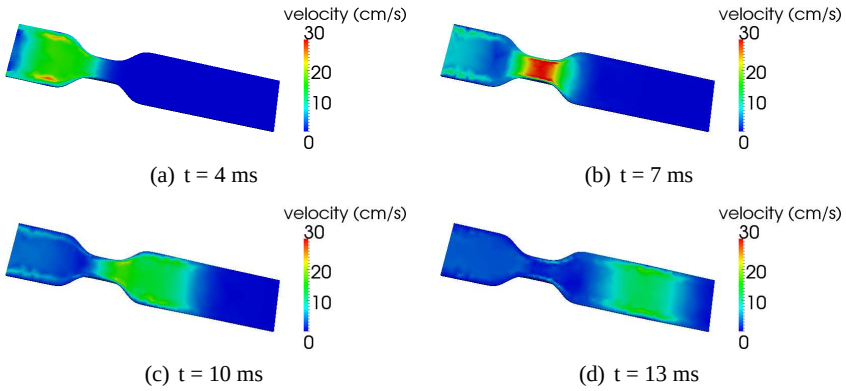

Fig. 16 A 2D cut of the 3D velocity through an asymmetric compliant stenotic region at four different times. The 2D cut plane is denoted in Fig. 15 by B. The corresponding pressure plots are shown in Fig. 18.

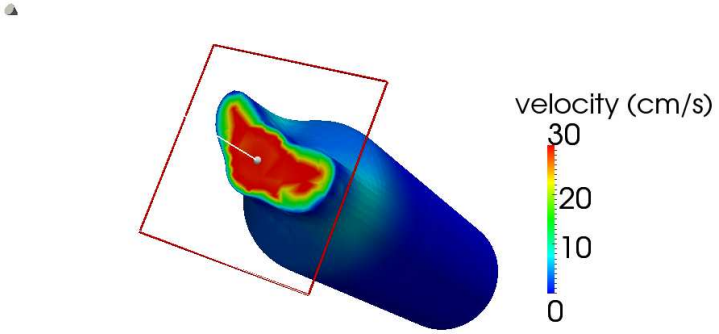

Fig. 17 A 2D cut of the 3D velocity at the stenotic throat at $t = 7$ ms. The 2D cut plane is denoted in Fig. 15 by A.

Finally, Fig. 19 shows the displacement of the structure at four different times. Notice how due to the high pressure in the proximal region to stenosis, the highest displacement can be observed exactly in that region. Within the stenotic region, the smallest displacement is observed at the most narrow part of the channel in the stenotic throat (visible at the bottom part of the stenotic throat in Fig. 19), where the velocity is highest. Notice also that the overall displacement at the distal site to stenosis if much smaller compared to that at the proximal region. The high pressure and high displacement in the region proximal to stenosis is an important piece of information from the clinical point of view. Namely, it has been reported in the medical literature (see, e.g., [24]) that the region most prone to the vulnerable plaque rupture is exactly the region proximal to the most stenotic region in a coronary artery.

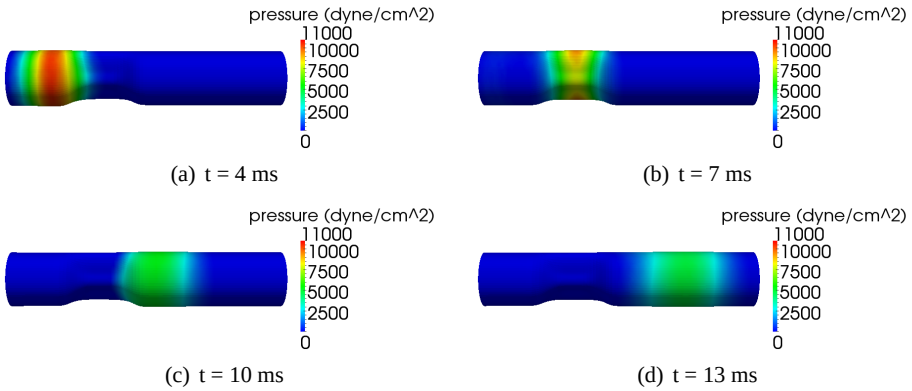

Fig. 18 Pressure in the asymmetric compliant stenotic region from Fig. 15, shown at four different times. The flow is from left to right.

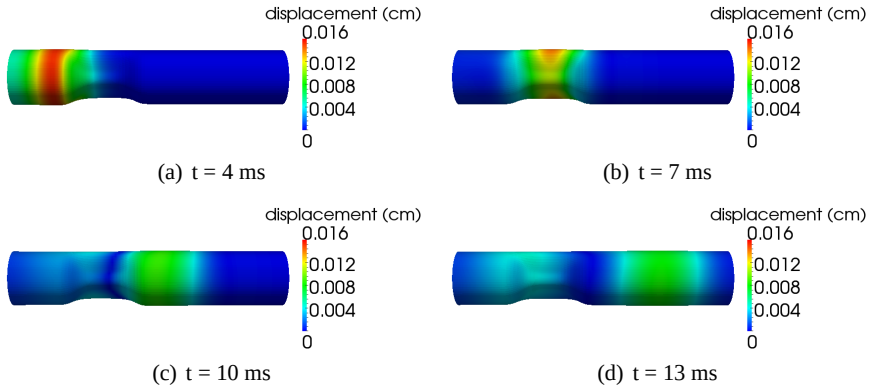

Fig. 19 Displacement in the asymmetric compliant stenotic region from Fig. 15, shown at four different times. The flow is from left to right.

6 Conclusions

In this chapter we presented a review of the kinematically-couped β-scheme as it applies to 3D fluid-structure interaction (FSI) problems between an incompressible, viscous, Newtonian fluid, and a thin, elastic structure modeled by the Koiter shell or membrane equations. This class of problems arises in computational hemodynamics modeling blood flow in compliant arteries. The proposed scheme is a loosely coupled partitioned scheme, which is based on the Lie operator splitting approach (or Marchuk-Yanenko scheme). Using this operator splitting approach, the multiphysics FSI problem is partitioned into a fluid and a structure sub-problem, which communicate in a way that makes the underlying partitioned scheme uncondition-

ally stable, without the need for sub-iterations between the two sub-problems at each time step. Using energy estimates, it was shown that the kinematically-coupled β-scheme is unconditionally stable, for all the parameters in the problem, even in the critical case of comparable fluid and structure densities. Several numerical examples were presented, including a 2D benchmark problem by Formaggia et al. [35], a pressure wave driven flow in a 3D straight tube, a pressure-driven flow in a 3D curved tube, and a problem describing a complex, stenotic geometry in 3D. Using numerical simulations it was shown that the kinematically-coupled β-scheme with $\beta = 1$ is at least first-order accurate in time. Modularity, low computational cost, and implementation simplicity make this scheme particularly appealing for the use in biofluidic FSI problems. Future developments include extensions of this scheme to study FSI with heart valves, FSI involving endovascular stents, and FSI involving composite structures.

Acknowledgements The authors would like to acknowledge Olivier Pironneau and Frédéric Hecht for a discussion regarding FreeFem++, and Simone Deparis for a suggestion regarding the numerical implementation of the coupling conditions. Many thanks to the National Science Foundation for partial research support under grants: DMS-1318763 (Bukač), DMS-1263572, DMS-1318763, DMS-1311709, DMS-1262385 and DMS-1109189 (Čanić), DMS-1311709 (Muha), and DMS-0914788 (Glowinski).

References

1. M. Astorino, F. Chouly, and M.A. Fernández. An added-mass free semi-implicit coupling scheme for fluid-structure interaction. *Comptes Rendus Mathématique*, 347(1-2):99–104, 2009.
2. M. Astorino, F. Chouly, and M.A. Fernández Varela. Robin based semi-implicit coupling in fluid-structure interaction: Stability analysis and numerics. *SIAM J. Sci. Comput.*, 31(6):4041–4065, 2009.
3. F.P.T. Baaijens. A fictitious domain/mortar element method for fluid-structure interaction. *Int. J. Numer. Meth. Fl.*, 35(7):743–761, 2001.
4. S. Badia, F. Nobile, and C. Vergara. Fluid-structure partitioned procedures based on Robin transmission conditions. *J. Comput. Phys.*, 227(14):7027–7051, 2008.
5. S. Badia, A. Quaini, and A. Quarteroni. Splitting methods based on algebraic factorization for fluid-structure interaction. *SIAM J. Sci. Comput.*, 30(4):1778–1805, 2008.
6. S. Badia, F. Nobile, and C. Vergara. Fluid-structure partitioned procedures based on Robin transmission conditions. year = 2008, *J. Comput. Phys.*, 227:7027–7051, 2008.
7. Y. Bazilevs, V.M. Calo, Hughes T.J.R, and Y. Zhang. Isogeometric fluid-structure interaction: theory algorithms and computations. *Comput. Mech.*, 43(1):3–37, 2008.
8. Y. Bazilevs, V.M. Calo, Y. Zhang, and Hughes T.J.R. Isogeometric fluid-structure interaction analysis with applications to arterial blood flow. *Comput. Mech.*, 38(4-5):310–322, 2006.
9. M. Bukač, S. Čanić, R. Glowinski, J. Tambača, and A. Quaini. Fluid-structure interaction in blood flow capturing non-zero longitudinal structure displacement. *Journal of Computational Physics*, 235:515–541, 2013.
10. M. Bukač, P. Zunino, and I. Yotov. Explicit partitioning strategies for interaction of the fluid with a multilayered poroelastic structure: An operator-splitting approach. *Submitted.*, 2013.
11. M. Bukač and S. Čanić. Longitudinal displacement in viscoelastic arteries: A novel fluid-structure interaction computational model, and experimental validation. *Journal of Mathematical Biosciences and Engineering*, 10(2):295–318, 2013.

12. M. Bukač, S. Čanić, R. Glowinski, B. Muha, and A. Quaini. A modular, operator splitting scheme for fluid-structure interaction problems with thick structures. *International Journal for Numerical Methods in Fluids*, Accepted 2013.
13. C.M. Colciago, S.Deparis, A.Quarteroni. Comparisons Between Reduced Order Models and Full 3D Models for Fluid-Structure Interaction Problems in Haemodynamics. *Journal of Computational and Applied Mathematics*
14. P. Causin, J.F. Gerbeau, and F. Nobile. Added-mass effect in the design of partitioned algorithms for fluid-structure problems. *Comput. Methods Appl. Mech. Eng.*, 194(42-44):4506–4527, 2005.
15. A. Chambolle, B. Desjardins, M. J. Esteban, and C. Grandmont. Existence of weak solutions for the unsteady interaction of a viscous fluid with an elastic plate. *J. Math. Fluid Mech.*, 7(3):368–404, 2005.
16. P. G. Ciarlet. A two-dimensional nonlinear shell model of koiter type. *C.R. Acad. Sci. Paris. Ser I Math.*, 331:405–410, 2000.
17. P. G. Ciarlet and D. Coutand. An existence theorem for nonlinearly elastic "flexural" shells. *J. Elasticity*, 50(3):261–277, 1998.
18. P. G. Ciarlet and A. Roquefort. Justification of a two-dimensional shell model of Koiter type. *C.R. Acad. Sci. Paris*, Ser I Math. 331(5):411–416, 2000.
19. C. M. Colciago, S. Deparis, and A. Quarteroni. Comparisons between reduced order models and full 3d models for fluid-structure interaction problems in haemodynamics. *Journal of Computational and Applied Mathematics*, Accepted, 2013.
20. G. H. Cottet, E. Maitre, and T. Milcent. Eulerian formulation and level set models for incompressible fluid-structure interaction. *ESAIM: Math. Model. Numer. Anal.*, 42(3):471–492, 2008.
21. S. Deparis, M. Discacciati, G. Fourestey, and A. Quarteroni. Fluid-structure algorithms based on Steklov-Poincaré operators. *Comput. Methods Appl. Mech. Engrg.*, 195(41-43):5797–5812, 2006.
22. S. Deparis, M. Fernandez, and L. Formaggia. Acceleration of a fixed point algorithm for a fluid-structure interaction using transpiration condition. *Math. Model. Numer. Anal.*, 37(4):601–616, 2003.
23. J. Donea. Arbitrary Lagrangian-Eulerian finite element methods. In *Computational Methods for Transient Analysis*. T. Belytschko and T.J.R. Hughes, eds., North-Holland, Amsterdam, 1983, 474–516.
24. E. Falk, P.K. Shah, and V. Fuster. Coronary plaque disruption. *Circulation*, 92(3):657–671, 1995.
25. H. Fang, Z. Wang, Z. Lin, and M. Liu. Lattice Boltzmann method for simulating the viscous flow in large distensible blood vessels. *Phys. Rev. E.*, 65(5):051925, 2002.
26. L.J. Fauci and R. Dillon. Biofluidmechanics of reproduction. In *Annu. Rev. Fluid Mech.*, volume 38, pages 371–394. Palo Alto, CA, 2006.
27. Z.G. Feng and E.E. Michaelides. The immersed boundary-lattice Boltzmann method for solving fluid-particles interaction problems. *J. Comp. Phys.*, 195(2):602–628, 2004.
28. M. A. Fernández and M. Moubachir. A Newton method using exact Jacobians for solving fluid-structure coupling. *Computers and Structures*, 83(2-3):127–142, 2005.
29. M.A. Fernández. Incremental displacement-correction schemes for the explicit coupling of a thin structure with an incompressible fluid. *Comptes Rendus Mathématique*, 349(7-8):473–477, 2011.
30. M.A. Fernández. Incremental displacement-correction schemes for incompressible fluid-structure interaction: stability and convergence analysis. *Numerische Mathematik*, 123(1):21–65, 2013.
31. M.A. Fernández, J.F. Gerbeau, and C. Grandmont. A projection algorithm for fluid-structure interaction problems with strong added-mass effect. *Comptes Rendus Mathematique*, 342(4):279–284, 2006.
32. M.A. Fernández and J. Mullaert. Displacement-velocity correction schemes for incompressible fluid-structure interaction. *Comptes Rendus Mathématique*, 349(17-18):1011–1015, 2011.

33. C.A. Figueroa, I.E. Vignon-Clementel, K.E. Jansen, T.J.R. Hughes, and C.A. Taylor. A coupled momentum method for modeling blood flow in three-dimensional deformable arteries. *Comput. Methods Appl. Mech. Eng.*, 195(41-43):5685–5706, 2006.
34. A.L. Fogelson and R.D. Guy. Platelet-wall interactions in continuum models of platelet thrombosis: Formulation and numerical solution. *Math. Med. Biol.*, 21:293–334, 2004.
35. L. Formaggia, J.F. Gerbeau, F. Nobile, and A. Quarteroni. On the coupling of 3d and 1d navier-stokes equations for flow problems in compliant vessels. *Comput. Methods Appl. Mech. Eng.*, 191(6-7):561–582, 2001.
36. J. Gerbeau and M. Vidrascu. A quasi-Newton algorithm based on a reduced model for fluid-structure interactions problems in blood flows. *Math. Model. Numer. Anal.*, 37(4):631–648, 2003.
37. R. Glowinski. Finite element methods for incompressible viscous flow. In *Handbook of Numerical Analysis*, volume IX. P.G.Ciarlet, J.-L.Lions eds., North-Holland, Amsterdam, 2003, 3–1176.
38. R. Glowinski, G. Guidoboni, and T.-W. Pan. Wall-driven incompressible viscous flow in a two-dimensional semi-circular cavity. *J. Comp. Phys.*, 216(1):76–91, 2006.
39. C. Grandmont. Existence of weak solutions for the unsteady interaction of a viscous fluid with an elastic plate. *SIAM J. Math. Anal.*, 40(2):716–737, 2008.
40. B.E. Griffith. Immersed boundary model of aortic heart valve dynamics with physiological driving and loading conditions. *Int. J. Numer. Methods Biomed. Eng.*, 28(3):317–345, 2012.
41. B.E. Griffith. On the volume conservation of the immersed boundary method. *Commun. Comput. Phys.*, 12(2):401–432, 2012.
42. B.E. Griffith, R.D. Hornung, D.M McQueen, and C.S. Peskin. An adaptive, formally second order accurate version of the immersed boundary method. *J. Comput. Phys.*, 223(1):10–49, 2007.
43. B.E. Griffith, R. Luo, D.M. McQueen, and C.S. Peskin. Simulating the fluid dynamics of natural and prosthetic heart valves using the immersed boundary method. *Int J Appl Mech.*, 1:137–177, 2009.
44. G. Guidoboni, R. Glowinski, N. Cavallini, and S. Čanić. Stable loosely-coupled-type algorithm for fluid-structure interaction in blood flow. *J. Comput. Phys.*, 228(18):6916–6937, 2009.
45. F. Hecht. Freefem++. `http://www.freefem.org/ff++/`.
46. F. Hecht. New development in FreeFem++. *J Numer. Math.*, 20:251–265, 2012.
47. M. Heil. An efficient solver for the fully coupled solution of large-displacement fluid-structure interaction problems. *Comput. Methods Appl. Mech. Eng.*, 193(1-2):1–23, 2004.
48. T.J.R. Hughes, W.K. Liu, and T.K. Zimmermann. Lagrangian-Eulerian finite element formulation for incompressible viscous flows. *Comput. Methods Appl. Mech. Eng.*, 29(3):329–349, 1981.
49. A. Hundertmark-Zaušková, M. Lukáčová-Medvidová, and G. Rusnáková. Fluid-structure interaction for shear-dependent non-Newtonian fluids. In *Topics in mathematical modeling and analysis*, volume 7. Matfyzpress, Prague, 109–158, 2012.
50. M.L. Irons. Curvature and geodesics of the torus. `http://www.rdrop.com/~half/math/torus/torus.geodesics.pdf`.
51. W. T. Koiter. On the foundations of the linear theory of thin elastic shells. i, ii. *Nederl. Akad. Wetensch. Proc.*, Ser. B 73:169–182, 1970.
52. M. Krafczyk, M. Cerrolaza, M. Schulz, and E. Rank. Analysis of 3D transient blood flow passing through an artificial aortic valve by Lattice-Boltzmann methods. *J. Biomech.*, 31(5):453–462, 1998.
53. M. Krafczyk, J. Tölke, E. Rank, and M. Schulz. Two-dimensional simulation of fluid-structure interaction using lattice-Boltzmann methods. *Comput. Struct.*, 79(22-25):2031–2037, 2001.
54. P. Le Tallec and J. Mouro. Fluid structure interaction with large structural displacements. *Comput. Methods Appl. Mech. Eng.*, 190(24-25):3039–3067, 2001.
55. A. Leuprecht, K. Perktold, M. Prosi, T. Berk, W. Trubel, and H. Schima. Numerical study of hemodynamics and wall mechanics in distal end-to-side anastomoses of bypass grafts. *J. Biomech.*, 35(2):225–236, 2002.

56. S. Lim and C.S. Peskin. Simulations of the whirling instability by the immersed boundary method. *SIAM J. Sci. Comput.*, 25(6):2066–2083, 2004.
57. Bukač M., S. Čanić, and Muha B. A partitioned scheme for fluid-composite structure interaction problems. *Under revision.*, 2014.
58. M. Galindo M. Cervera, R. Codina. On the computational efficiency and implementation of block-iterative algorithms for nonlinear coupled problems. *Engrg. Comput.*, 13:4–30, 1996.
59. A. Hundertmark-Zaušková M. Lukáčová-Medvid'ová, G. Rusnáková. Kinematic splitting algorithm for fluid-structure interaction in hemodynamics. *Computer Methods in Appl. Mech. Engi.*, 265:83–106, 2013.
60. H. Matthies and J. Steindorf. Numerical efficiency of different partitioned methods for fluid-structure interaction. *Z. Angew. Math. Mech.*, 2(80):557–558, 2000.
61. C. Michler, S.J. Hulshoff, E.H. Van Brummelen, and R. De Borst. A monolithic approach to fluid-structure interaction. *Computers and Fluids*, 33(5):839–848, 2004.
62. L.A. Miller and C.S. Peskin. A computational fluid dynamics study of 'clap and fling' in the smallest insects. *J. Exp. Biol*, 208(2):195–212, 2005.
63. B. Muha and S. Čanić. Existence of a weak solution to a fluid-structure interaction problem motivated by blood-artery-stent interaction. In preparation. 2013.
64. B. Muha and S. Čanić. Existence of a weak solution to a nonlinear fluid-structure interaction problem modeling the flow of an incompressible, viscous fluid in a cylinder with deformable walls. *Arch. Ration. Mech. Anal.*, 207(3):919–968, 2013.
65. B. Muha and S. Čanić. Existence of a weak solution to a fluid-multi-layered-structure interaction problem. *Journal of Differential Equations*, 256:658–706, 2014.
66. B. Muha and S. Čanić. A nonlinear, 3D fluid-structure interaction problem driven by the time-dependent dynamic pressure data: a constructive existence proof. *Communications in Information and Systems*, 13(3):7555, 2014.
67. C.M. Murea and S. Sy. A fast method for solving fluid-structure interaction problems numerically. *Int. J. Numer. Meth. Fl.*, 60(10):1149–1172, 2009.
68. F. Nobile. *Numerical Approximation of Fluid-Structure Interaction Problems with Application to Haemodynamics*. PhD thesis, Department of Mathematics, Federal Institute of Technology, Lausanne, Switzerland, 2001.
69. F. Nobile and C. Vergara. An effective fluid-structure interaction formulation for vascular dynamics by generalized Robin conditions. *SIAM J. Sci. Comput.*, 30:731–763, 2008.
70. C.S. Peskin. Numerical analysis of blood flow in the heart. *J. Computational Phys.*, 25(3):220–252, 1977.
71. C.S. Peskin and D.M. McQueen. Modeling prosthetic heart valves for numerical analysis of blood flow in the heart. *J. Comput. Phys.*, 37(1):113–132, 1980.
72. A. Quaini. *Algorithms for Fluid-Structure Interaction Problems Arising in Hemodynamics*. PhD thesis, Department of Mathematics, Federal Institute of Technology, Lausanne, Switzerland, 2009.
73. A. Quaini and A Quarteroni. A semi-implicit approach for fluid-structure interaction based on an algebraic fractional step method. *Math. Models Methods Appl. Sci.*, 17(6):957–985, 2007.
74. A. Quarteroni, M. Tuveri, and A. Veneziani. Computational vascular fluid dynamics: problems, models and methods. *Comput. Vis. Sci.*, 2(4):163–197, 2000.
75. J. Tambača, S. Čanić, and A. Mikelić. Effective model of the fluid flow through elastic tube with variable radius. *Grazer Mathematische Berichte*, 348:91–112, 2005.
76. R. Van Loon, P.D. Anderson, J. De Hart, and F.P.T. Baaijens. A combined fictitious domain/adaptive meshing method for fluid-structure interaction in heart valves. *Int. J. Numer. Meth. Fl.*, 46(5):533–544, 2004.
77. I. Velčić Private communication.
78. S. Čanić, B. Muha, and M. Bukač. Stability of the kinematically coupled β-scheme for fluid-structure interaction problems in hemodynamics. *Journal for Numerical Analysis and Modeling*, In print, 2014, arXiv:1205.6887.
79. S. Zhao, X. Xu, and M. Collins. The numerical analysis of fluid-solid interactions for blood flow in arterial structures, Part 2: Development of coupled fluid-solid algorithms. *Proc. Instn. Mech. Eng. Part H*, 212:241–252, 1998.